# Developmental Synchrony of Retinal Waves, Apoptosis, and Angiogenesis in Postnatal Retina

Michael A. Savage[1*], Cori Bertram[1], Jean de Montigny[1,3], Courtney A. Thorne[1,4], Rachel Queen[1], Majlinda Lako[1], Gerrit Hilgen[1,2*], Evelyne Sernagor[1]

1. Biosciences Institute, Faculty of Medical Sciences, Newcastle University, UK
2. School of Geography and Natural Sciences, Northumbria University, United Kingdom, UK
3. Current address: Institute of Neuroscience of Montpellier, Inserm 1298, Montpellier, France
4. Current address: Faculty of Medical and Health Sciences, Medical Sciences, University of Aukland, New Zealand

*Joint corresponding authors

Dr Michael A Savage

michael.savage2@newcastle.ac.uk

Biosciences Institute, Faculty of Medical Sciences, Newcastle University, UK

Dr Gerrit Hilgen

gerrit.hilgen@northumbria.ac.uk

Northumbria University, Ellison Place, United Kingdom, NE1 8ST, UK

Keywords: Retina, development, microglia, angiogenesis, apoptosis, widefield calcium imaging, neonatal mouse

## Abstract

Postnatal mouse retinal development is a multi-faceted process involving the coordinated interaction of spontaneous neural activity as retinal waves, vascular plexus growth, and programmed cell death. While these processes are known to interact at a coarse scale, the specific mechanisms integrating them have remained elusive. Using large-scale, widefield calcium imaging, high-density multielectrode array recordings, single cell RNA-seq, and immunohistochemistry, we characterise a tightly aligned centrifugal expansion pattern during retinal development. This pattern is common to stage II retinal wave onsets, vascular development, Heme oxygenase-1 (Hmox1) expressing microglia, apoptotic cell markers, and

a novel set of auto-fluorescent cluster complexes (ACCs) identified in this study. Apoptotic cells are known to upregulate functional Pannexin1 (PANX1) hemichannels. These voltage-gated channels release purinergic molecules which act as “eat me” signals to neighbouring microglia. PANX1 hemichannel blockade with the drug probenecid results in a profound decrease in spontaneous wave frequency and strength, suggesting that retinal waves are indeed triggered by these apoptotic cells.

Taken together, our observations suggest that spontaneous waves are initially triggered in hotspots by hyperactive apoptotic RGCs in unvascularised retinal areas. These apoptotic cells release purinergic molecules via PANX1 hemichannels, leading to wave generation. This hyperactivity leads to local hypoxic conditions, which, coupled with high extracellular ATP concentrations, promotes angiogenesis. Once blood vessels reach a particular hotspot, ATP release activates Hmox1 positive microglia, which engulf the dying RGCs, creating the auto-fluorescent clusters. We suggest that these early occurring events may be universal in the developing CNS, causally linking early neural activity, programmed cell death and angiogenesis.

## Introduction

Spontaneous neural activity is a hallmark of developing neural tissue (O’Donovan, 1999). This is ubiquitous across species and present in both the peripheral and central nervous systems. In the retina, this takes the form of waves of electrical activity that sweep across the retinal ganglion cell (RGC) layer. It occurs during very precise and restricted temporal windows, overlapping with other important developmental events such as cell differentiation, programmed cell death, neurite outgrowth, synapse formation and angiogenesis. This activity occurs in three consecutive stages with unique circuit and pharmacological involvement. They are first mediated by gap junctions between RGCs as embryonic Stage I (Bansal et al., 2000; Catsicas et al., 1998; Syed, Lee, He, et al., 2004). Stage I waves are followed by Stage II waves, which are mediated by cholinergic synaptic transmission through starburst amacrine cells (SACs) and last until postnatal day (P)10 (Bansal et al., 2000; Catsicas et al., 1998; Feller et al., 1996; Sernagor et al., 2000, 2003; Sernagor & Grzywacz, 1996, 1999; Syed, Lee, Zheng, et al., 2004; Wong et al., 1998; Zhou & Zhao, 2000). Finally, glutamatergic signalling through bipolar cells governs Stage III waves until eye opening at P15 (Bansal et al., 2000; Blankenship et al., 2009; Syed, Lee, Zheng, et al., 2004; Zhou & Zhao, 2000). While the role of spontaneous activity in refining network connectivity is well-documented, the endogenous factors that initiate and spatially constrain these waves, particularly their link to non-neuronal maturation, remain largely unexplored.

During the first postnatal week, concurrent with stage II waves, the mouse retina undergoes angiogenesis, with the superficial vascular plexus extending from the optic nerve head towards the peripheral retina. This process begins at P0, with blood vessels extending radially until around P7, when they reach the retinal periphery (Paredes et al., 2018). Their growth is guided by the metabolic needs of the tissue, with local hypoxia and gradients in metabolic demand driving the expansion of the vascular plexus (Chan-Ling et al., 1995; Gariano & Gardner,

2005). This pro-angiogenic drive is evident during Stage II retinal wave activity, which increases in size and frequency from P2 before declining sharply at P7 (Maccione et al., 2014; Weiner et al., 2019). The expansion of the vascular bed plays a crucial role in establishing healthy vascular architecture during retinal maturation and beyond.

Microglia have been shown to have an intimate connection to the progression of vascular development in the retina. They localise to the endothelial tip cells and interact with the developing vasculature endothelium (Liu et al., 2026). A specific subgroup of microglia expressing the *Homx1* gene has been shown to display an annular pattern of distribution around the growing vascular plexus edge (Martineau et al., 2026). Depleting microglia leads to a significant decrease in expansion and density of retinal blood vessels, and reintroduction of microglia results in reversal and recovery of the superficial vascular plexus (SVP) (Checchin et al., 2006).

Furthermore, developmental apoptosis in the murine retina follows a centrifugal wave pattern mirroring both vascular growth and the microglial annulus. These large apoptotic waves peak during the first postnatal week, after which apoptotic marker gene expression transiently declines at P7 (Anderson et al., 2019; Farah & Easter, 2005). This process is functionally linked to remodelling via signalling molecules such as ATP, which is released through PANX-1 hemichannels and acts as a dual-purpose driver. It triggers angiogenesis while simultaneously serving as an 'eat-me' signal that transforms quiescent, ramified microglia into the amoeboid, phagocytic state required to engulf dying cells.

While retinal wave progression, developmental apoptosis, and angiogenesis occur concurrently in the postnatal mouse retina, existing literature lacks a cohesive framework that accounts for their interdependence. Despite their overlapping timelines, these processes are frequently studied in isolation, leaving the functional links between neural activity, cell death, and vascularisation largely unexplored.

In this study, we identify a novel population of auto-fluorescent cluster complexes (ACCs) that form an annulus beneath the leading edge of the superficial vascular plexus (SVP) during the P0–P7 developmental window. Our data reveal that these ACCs, which disappear upon vascular arrival at the periphery, consist of apoptotic retinal ganglion cells (RGCs) engulfed by specialised microglia. Using a multi-modal approach, including electrophysiology, calcium imaging, single cell (sc) RNA-Seq, and microglial tracking, we demonstrate that retinal wave initiation points shift peripherally in perfect spatiotemporal correlation with SVP expansion and programmed cell death (PCD). Crucially, we show that apoptotic RGCs trigger Stage II wave initiation; the resulting intense bursting creates a localised metabolic demand that recruits blood vessels to the area. Simultaneously, these apoptotic RGCs release purinergic signals via PANX-1 hemichannels, marking them for microglial phagocytosis and generating the characteristic auto-fluorescent ACCs. Together, these results provide a unified framework for the timely vascularisation of the postnatal retina.

## Results

## Centrifugal Expansion Pattern is Shared Between ACCs and Vascular Development in Postnatal Mouse Retina

The hypothesis that retinal waves, apoptosis, and angiogenesis are synchronised in the developing retina emerged from the discovery of sparse ACCs, which form a distinct, tight annulus around the optic nerve head (ONH) at P2–3 (Figure 1A). These ACCs appear sequentially in eccentricity outward from P2, disappearing at the retinal periphery by P7. This distribution precisely mirrors the expansion of the SVP, which extends from the ONH toward the periphery between P7 and P9 (Figure 1A, B, G). The ACCs exhibit broad-spectrum fluorescence across multiple wavelengths (Figure 1C and are situated in close proximity to, but do not overlap with, starburst amacrine cells (SACs; Figure 1D). These cells are localised exclusively within the ganglion cell layer (GCL) and are entirely absent from the inner nuclear layer (INL; Figure 1F). Notably, the ACCs consistently trail the leading edge of the vascular front across all developmental stages, with peak activity observed between P2 and P3, suggesting a mechanistic role in SVP guidance (Figure 1G). Quantitative analysis further reveals significantly elevated blood vessel branching in ACC-associated regions compared to equivalent eccentricities where ACCs are absent (Figure 1E). To characterise the molecular identity of these cells and their potential role in synchronising retinal waves with angiogenesis, we performed single-cell RNA sequencing (scRNA-seq).

## Single-Cell RNA-Seq Reveals Auto-fluorescent Cell Complexes as Microglia and Dying RGC Aggregates in the Postnatal Mouse Retina

ACCs were enriched using flow activated cells sorting (FACS) and subjected to scRNA-Seq, which revealed the presence of five distinct clusters (Figure 2A). Following FACS, the cell suspension was centrifuged to meet the input requirements of the 10x Genomics microfluidic platform, resulting in an estimated ~50% reduction in yield. Haemocytometer quantification indicated that 9,405 viable single cells were loaded onto the 10x chip. Given an expected capture efficiency of ~50%, approximately 5,000 FACS-purified cells were recovered for scRNA-seq library preparation. Libraries were generated and sequenced to a depth of 50,000 reads per cell using Illumina technology.

Unsupervised clustering and UMAP visualisation identified five distinct cell populations (Figure 2A). Cluster 0 was identified as microglia, exhibiting high expression of canonical markers including *Aif1*, *Sparc*, *C1qb*, *Sall1*, *P2ry12*, *Cd68*, *Dock10*, and *Cx3cr1* (Figure 2B). Cluster 1 comprised endothelial cells, as evidenced by the expression of *F13a1* and *Dab2* (Figure 2C). Clusters 2 and 3 represented cycling populations: Cluster 2 was characterised by microtubule dynamics genes (*Stmn1*, *Tubb3*; Figure 2D), while Cluster 3 consisted of retinal progenitor cells (RPCs) expressing proliferation markers such as *Top2a* and *Cdk1* (Figure 2E). Cluster 4 was identified as neurogenic progenitors based on the expression of *Rorb* and *Neurod1* (Figure 2F).

Notably, the whole dataset exhibited high levels of the apoptotic marker *Bax* and the RGC-specific marker *Rbpms* (Figure 2G), suggesting a transcriptomic signature for ACCs consistent with RGC apoptosis and engulfment by microglia. A comprehensive list of cluster-specific markers is provided in Supplementary Table A.

## Microglia Are Attracted to ACCs in the Postnatal Mouse Retina

Given that scRNA-Seq analysis identified a prominent microglial component within ACCs, we next examined whether microglial distribution in situ was spatially coupled to the presence of ACCs. Immunolabelling for the microglial marker *Iba-1* demonstrated strong co-localisation between microglial cells and ACCs (Figure 3A). Quantitative analysis confirmed that microglial density was significantly elevated in ACC-associated regions compared with matched retinal areas lacking clusters ($p = 0.0138$). Across retinas, microglial density significantly increased when associated with ACCs (Figure 3B, $p=0.0318$), and there was a strong positive correlation observed between microglial cell density and ACC cell density (Figure 3C, $p < 0.0001$).

Because microglial density varies as a function of retinal eccentricity during postnatal development, we assessed whether enrichment at ACC sites could be explained by underlying radial gradients. Regions of interest were sampled at four progressively increasing eccentricities from the optic nerve head (ONH), with paired regions defined as ACC-positive (ACC+) or ACC-negative (ACC−) (Figure 3D). Consistent with developmental migration patterns, microglial density increased closer to the ONH in all samples (Figure 3E). However, when eccentricity was controlled, microglial enrichment was restricted to regions directly co-localised with ACCs. Only regions positioned at the same radial distance as the ACC annulus exhibited significantly elevated microglial density relative to matched ACC− regions (Figure 3E, "@ Cluster", $p<0.01$). Areas located either peripheral ("ahead") or central ("behind") relative to ACC positions did not show a comparable increase (Figure 3E).

## Hmox1-positive Microglia Target Apoptotic RGCs through a PANX1-Purinergic Signalling Axis

To investigate these findings further, we specifically interrogated a subset of *Hmox1*-expressing microglia. This population has been previously implicated in vascular development and remodelling, particularly in the context of retinal maturation (Martineau et al., 2026). This subset of microglia exhibits a similar annular expansion pattern during the first postnatal week to that of the ACCs and SVP (Figure 4A). These microglia straddle the vascular margin, extending processes both ahead of and behind the vessels. In these regions, they maintain direct contact with ACCs and exhibit clear evidence of engulfment, with ACC material localised within intracellular vesicles (Figure 4C).

Microglial activation is frequently driven by the sensing of environmental purinergic molecules. Specifically, apoptotic cells release ATP via voltage-gated Pannexin-1 (PANX1) hemi-channels, which is sensed by microglial P2Y12 receptors. To determine if this signalling axis contributes to ACC formation, we utilised the apoptotic marker YO-PRO-1, which selectively enters cells through open PANX1 channels. Wholemount staining revealed a broad centro-peripheral gradient of apoptosis; however, this apoptotic annulus was positioned more peripherally than the ACCs, SVP, and *Hmox1*-positive microglia (Figure 4B).

High-resolution immunohistochemistry further demonstrated that these apoptotic cells localise within the same intracellular vesicles as the ACCs (Figure 4C, D). Co-staining with Rbpms and

198 ChAT confirmed the identity of these YO-PRO-1-positive cells as RGCs rather than SAC
199 (Figure 4E, F). Finally, we observed a precise spatial alignment between PANX1 expression
200 and YO-PRO-1-positive cells, which together form an ACC-like organisation in the developing
201 retina (Figure 4G, H).

202 **Purinergic Signalling Modulation Drastically Affects Hmox1 Microglia Activation and**
203 **ACC Formation**

204 Hmox1 microglia activation is mediated via purinergic signalling through PANX-1
205 hemichannels in apoptotic cells, acting as a 'find me, eat me' signal. This ATP sensing is carried
206 out by P2Y12 receptors on the microglial cell surface. To investigate and verify this fully, we
207 examined the effects of blocking either ATP release through the PANX-1 channels with
208 probenecid or ATP sensing from microglia via P2Y12 receptors with PSB-0739. Overnight
209 incubation of the retinal wholemounts with probenecid or PSB-0739 had dramatic effects on
210 Hmox1 microglial activation across all morphometric parameters. Blocking either purinergic
211 release or sensing, shifted Hmox1 microglia into a significantly more ramified or less activated
212 state. This in short significantly decreased circularity, increased perimeter, increased total
213 skeleton length and number of branch points (Figure 5A-D). These changes in morphology are
214 visually apparent in Figure 5J-L.

215 Blockade of purinergic signalling also had a noticeable effect on the numbers of Hmox1
216 microglia and YO-PRO-1 positive cells. The number of Hmox1 microglia found in the retina
217 increased across the board, although only probenecid 2mM displayed a significant increase
218 (Figure 5E). Unsurprisingly, blocking release or uptake of ATP drastically reduced the number
219 of YO-PRO-1 positive cells, but with probenecid treatment, this may be a mechanistic effect
220 of blocking the PANX-1 channels (Figure 5F). Similarly, the number and percentage of Hmox1
221 microglia containing apoptotic cell fragments in their vesicles also decreased after blockade.
222 However, this only reached significance with probenecid treatment (Figure 5G, H). Blocking
223 purinergic signalling did not seem to have any effect on the percentage of YO-PRO-1 positive
224 cells, which were colocalised with Hmox1 microglia (Figure 5I).

225 In addition to morphometrics and cell frequency changes, we also examined the peripherality
226 of YO-PRO-1 positive cells after drug application. To normalise the apoptotic cell locations to
227 account for the changing retina size we converted the origin locations into the D1/2metrics.
228 These metrics showed no significant changes but there was a trend for probenecid-treated
229 retinas to display a broader apoptotic distribution, with a shift toward the retinal periphery. On
230 the other hand, D1/3 metrics displayed a significant shift of the YO-PRO-1 positive cells
231 treated with PSB-0739 away from the SVP edge and the peripheral non-vascularised areas
232 towards the central retina (Figure 5M, N).

233 **Stage II Retinal Waves Display Centrifugal Expansion and Modulation by Purinergic**
234 **Signalling**

235 Because ACCs are present exclusively during the period of Stage II retinal waves, we
236 hypothesised a link between these clusters and wave generation or propagation. To test this, we
237 performed whole-mount calcium imaging on IB4-labelled retinas to map wave origination
238 points and quantify wave metrics relative to the vasculature. Representative calcium imaging

239 and wave activity plots are shown in Figure 6A, B. By aligning functional activity with
240 anatomical landmarks, we mapped all wave origination points relative to the SVP in the P4
241 retina (Figure 6C) and visualised the spatial coverage of individual waves (Figure 6D). Given
242 the tight anatomical association between ACCs and apoptotic cells expressing PANX1
243 hemichannels, we next investigated whether blocking purinergic release altered wave
244 dynamics.

245 Treatment with 1 mM probenecid, a potent PANX1 inhibitor, profoundly attenuated nearly all
246 measured wave metrics. Specifically, wave frequency (Figure 6G), speed (Figure 6I), and total
247 path length (Figure 6J) were significantly reduced upon drug application. While probenecid
248 treatment led to a significant decrease in wave area at P3, P5, and P6, P4 retinas uniquely
249 exhibited a significant increase in this metric (Figure 6H).

250 Across all postnatal ages, the majority of retinal waves originated in the peripheral regions.
251 These wave initiation points exhibited a centrifugal expansion pattern mirroring the
252 progression of the ACCs, vasculature, and microglia. Between P3 and P6, wave origins
253 demonstrated a significant increase in relative peripherality (D1/D2; Figure 6E). This
254 peripheral bias was even more pronounced when origins were normalised to the vascular
255 margin; wave initiation was significantly more likely to occur within non-vascularized regions
256 across all stages (Figure 6F). Indeed, the median D1/D3 value, representing the position
257 relative to the vascular front; only approached 1 at P6, when the retina is nearly fully
258 vascularised.

259 **Synchronised Centrifugal Expansion Pattern Across Multiple Developmental Processes**

260 To examine the overall developmental expansion pattern, we extended the use of the D1/2
261 metrics across retinal wave generation, vascular growth, apoptotic activity, and microglial
262 positioning. Visualising the relative positions of these processes highlights a strongly
263 conserved organisation (Figure 7). Spontaneous wave initiation points, recorded via MEA
264 (orange) or calcium imaging (cyan), predominantly emerge within the non-vascularized
265 periphery and shift further toward the retinal margin between P3 and P6. This centrifugal
266 progression converges at P6 as the SVP achieves near-total coverage. Similarly, the density of
267 apoptotic cells (YO-PRO-1; blue) shifts peripherally over this period. Notably, the expansion
268 of the SVP (magenta) consistently lags behind the wave initiation front, while the Hmox1+
269 microglial annulus (red) straddles both the vascular border and the ACC positions. Throughout
270 development, ACCs maintain the most central position relative to these expanding fronts until
271 P6, when they eventually reach the retinal periphery (brown).

272 In summary, these data reveal a precisely orchestrated spatiotemporal sequence in the
273 developing retina, where a peripheral wave of neuronal activity and RGC apoptosis
274 consistently precedes vascular expansion. The stable spatial relationship between Hmox1-
275 positive microglia, ACCs, and the trailing vascular front suggests that the outward migration
276 of the SVP is not a stochastic process, but rather one guided by a pre-patterned landscape of
277 purinergic signalling and phagocytic remodelling. This 'wave-front' architecture ensures that
278 metabolic demand and neuronal maturation are tightly coupled with the emerging blood supply
279 during the first postnatal week.

## Discussion

Herein, we demonstrate for the first time clusters of auto-fluorescent cell complexes which are found in mouse retina over the first postnatal week. Investigating their nature and composition has revealed a tightly regulated synchrony of multiple developmental processes and illuminated several new insights in retinal development and angiogenesis, Figure 8A-C. Dying RGCs in the periphery release purinergic molecules, which help initiate retinal waves and act as a proangiogenic marker, which in turn helps guide the outward expansion of the vascular plexus. This vascular wavefront is coordinated by a distinct microglial annulus that actively monitors the retinal environment Figure 8B. Upon contact, these microglia initiate the phagocytic clearance of apoptotic RGCs, resulting in the formation of ACCs, a process that effectively pre-patterns the retinal landscape for subsequent vascular expansion Figure 8C.

More specifically, we have uncovered a developmental gradient that expands in a centrifugal manner from the ONH. We discovered that apoptosis of developing RGCs promotes the expression of PANX-1 hemichannels. These dying cells release a host of purinergic molecules such as ATP through the PANX-1 hemichannels. ATP acts to promote the initiation of retinal waves; blocking these PANX-1 channels greatly reduces the frequency and size of the waves. The apoptotic cells and wave initiations are more prevalent in the peripheral non-vascularised zones of the retina. The purinergic release and energy demand of wave initiations, in turn, act as a proangiogenic signal which drives the expansion of the SVP. A specialised subset of microglia expressing *Hmox-1* site astride the SVP edge and help guide the growth of endothelial tip cells. They also have a strong phagocytotic role, where they engulf apoptotic RGCs under the vascularised area. Our findings indicate that microglia engulf apoptotic RGCs and sequester them within phagocytic vacuoles for degradation, thereby forming the ACCs that initially prompted this investigation. This model is further supported by our observation that vascular maturation is significantly more advanced in retinal regions where ACCs are present, suggesting these aggregates serve as a focal point for angiogenesis.

It is surprising that ACCs have remained unidentified until now, given their highly stereotyped progression pattern. However, well-documented autofluorescence from cellular debris and molecules such as lipofuscin (Kennedy et al., 1995; Sparrow, 2007) and drusen (Imamura et al., 2006; Spaide & Curcio, 2010) likely confounded previous attempts at identification. Their relative sparsity may have further led to their misclassification as non-specific staining, underscoring the necessity of pan-retinal visualization for reliable detection. Furthermore, their intrinsic autofluorescence complicates traditional immunohistochemical characterization. By leveraging scRNA-seq, we bypassed these optical limitations to reveal the molecular identity of ACCs as multicellular aggregates comprising microglia, apoptotic RGCs, and endothelial components.

The transcriptomic profile of the largest cell cluster (cluster 0) identifies these microglia as central orchestrators of postnatal retinal development. High expression of canonical markers, including *Aif1*, *P2ry12*, *C1qb*, and *Sall1*, reflects a specialised homeostatic state geared toward neurovascular interaction and phagocytic refinement. Specifically, the co-expression of

microglial markers with RGC-specific *Rbpms* (Rodriguez et al., 2014) and apoptotic regulators (*Bax*) provides molecular evidence for the active clearance of RGCs (Edlich et al., 2011; Han et al., 2001). This process is likely driven by a *P2ry12*-mediated purinergic response to apoptotic signals and local hypoxia, with *Aif1* (Iba1) facilitating the necessary phagocytic cup formation.

Beyond debris clearance, the enrichment of *C1qb* and *Sparc* suggests these cells are actively involved in activity-dependent synaptic tagging and migratory modulation, respectively. Meanwhile, the maintenance of *Sall1* expression indicates that while these microglia are highly active in remodelling, they retain a non-reactive, developmental identity. Collectively, these data support a model where Cluster 0 microglia integrate purinergic sensing and complement-mediated refinement to facilitate the precise spatiotemporal maturation of the retinal landscape.

A significant outcome of this study is the discovery that Stage II retinal wave initiation follows a highly stereotyped, centrifugal expansion pattern. This observation stands in sharp contrast to the prevailing consensus in the field, which has historically characterised wave initiation as a stochastic or random process (Blankenship & Feller, 2010; Firth et al., 2005; Maccione et al., 2014; Stafford et al., 2009; Zheng et al., 2006). Notably, our data indicate that wave origins are consistently biased toward non-vascularised peripheral regions throughout the first postnatal week. While these findings refuted our initial hypothesis that ACCs serve as the primary source of wave initiation, it reveals a previously unrecognised topographical coordination between neuronal activity and retinal maturation. This spatial bias suggests that the "active" zone of the developing retina is defined by the absence of vasculature, potentially linking wave dynamics to local metabolic or purinergic gradients.
Wave-like activity from the retina propagates to the rest of the visual system and are known to help form the proper retinotopy or world view in both V1 and the superior colliculus (SC) (Ackman et al., 2012; Blankenship & Feller, 2010; Firth et al., 2005). Previous *in vitro* retinal MEA recordings has shown that there is a propagation bias for retinal waves to travel along the nasal-temporal axis (Stafford et al., 2009). This direction bias is maintained through the SC and V1 (Ackman et al., 2012). However, none of these studies noted anything that resembled the centrifugal progression pattern described here. It follows that the centrifugal expansion of wave initiations may aid in the progressive development of the entire visual processing circuit throughout the brain. Focusing the retinal activity origins in concentric annuli ensures that the visual system develops from the central to peripheral retina representations. It follows that this pattern of progression may have a large effect of the develop of the retinotopic map in the higher areas but that is beyond the scope if this research.

Several methodological factors likely explain why these developmental mechanisms remained previously undetected. First, our use of high-density Microelectrode Arrays (MEAs) provided superior spatial sampling and comprehensive pan-retinal coverage compared to the sparser configurations used in earlier studies. This was complemented by wide-field calcium imaging, which enabled us to localise wave dynamics with micron-scale precision and directly correlate them with the advancing SVP margin. Furthermore, while previous research often pooled data across the first postnatal week, thereby masking developmental shifts, our daily longitudinal analysis preserved the fine-tuned organisation of wave initiation. By avoiding the loss of

temporal resolution inherent in data aggregation, we were able to resolve the centrifugal progression that is otherwise collapsed in cross-sectional or pooled datasets.

A defining feature of this research is the remarkable synchrony observed between neuronal activity, programmed cell death, and angiogenesis. By utilising normalised peripherality metrics (D1/D2), we demonstrated that these processes are not merely concurrent but are strictly organised into a mobile "wavefront" that traverses the retina. Throughout the first postnatal week, retinal wave initiation is consistently sequestered within the non-vascularised periphery, shifting further toward the retinal margin in lockstep with the expanding vasculature.

This advancing front is preceded by an annulus of apoptotic RGCs (YO-PRO-1+), the majority of which reside immediately ahead of the SVP. Positioned precisely at this interface, a specialised subset of Hmox1+ microglia straddles the leading edge of the vascular plexus. These microglia actively engulf the dying RGCs, sequestering them within intracellular vacuoles to form the ACCs. Our genetic and histological evidence confirms that ACCs are the direct product of this phagocytic interaction, located strategically beneath the growing vascular margin. This highly ordered spatial hierarchy persists until P6, at which point the developmental annuli converge at the retinal periphery, signalling the completion of this primary maturation phase.

Our findings highlighted the importance of purinergic signalling through PANX-1 hemichannels in the integrated development of the retina. Modulation of purinergic signalling has been shown to drastically affect retinal wave dynamics, (Stellwagen et al., 1999) but its' source was not identified. From our work it seems likely that apoptotic RGCs are a great candidate for this modulation. Purinergic molecules are released through PANX1 hemichannels, which are found in high levels on mature RGCs (Bao et al., 2004; Dvoriantchikova et al., 2006). Sensing extracellular purinergic markers through P2 receptors is the major molecule responsible for transitions from quiescent to activated phagocytotic microglia (Fontainhas et al., 2011; Velasquez & Eugenin, 2014).

The discovery of this integrated mechanism in the retina raises the compelling possibility that a similar "wavefront" governs development across the entire Central Nervous System (CNS). Auto-fluorescent inclusions within microglia, reminiscent of ACCs, have been observed in the ageing brain (Stillman et al., 2023), while purinergic signalling is already known to modulate spontaneous activity in the developing auditory system (Babola et al., 2021). Our findings suggest a universal developmental logic: the programmed over-proliferation of neurons creates a metabolic and purinergic gradient that directs vascular expansion, fine-tuned by specialised microglial activity.

This theory is bolstered by striking temporal correlations elsewhere in the CNS. In the mouse spinal cord, the peak of apoptosis at E12–E13 aligns precisely with the invasion of vessels into deep tissue layers(Nakao et al., 1988; Yamamoto & Henderson, 1999). Similarly, cortical apoptosis at E14 coincides with vascular infiltration from the subventricular plexus (Chen et al., 2017; Gupta et al., 2021; Kuan et al., 2000). We propose that in these regions, Hmox1-positive microglia may perform the same "double duty" observed in the retina: clearing superfluous apoptotic cells while simultaneously harnessing purinergic signals to guide angiogenesis and synchronise neural activity. Ultimately, our work highlights the necessity of

405 a holistic, multi-system approach to resolve how neural activity and vascular architecture are
406 co-constructed during development.

# 407 Methods

## 408 Characterisation of Auto-fluorescent Cluster Complexes

409 *Cell Dissociation*

410 Dissected retinas from P5 C57BL/6 mice were kept in oxygenated artificial cerebrospinal fluid
411 aCSF (118mM NaCl, 25mM $NaHCO_3$, 1mM $NaH_2PO_4$, 3mM KCl, 1mM $MgCl_2$, 2mM $CaCl_2$,
412 and 10mM glucose) until they were dissociated using the Neurosphere Dissociation Kit (P)
413 (Miltenyi Biotec GmbH, Teterow, Germany (103-095-943)), in accordance with the
414 manufacturer's instructions.

415 *Fluorescence Activated Cell Sorting (FACS)*

416 FACS polypropylene collection tubes were pre-coated with 20% FBS overnight at 4 °C prior
417 to use. Dissociated cells were suspended in 2% foetal bovine serum (FBS) in the pre-coated
418 tubes. 5% FBS collection buffer was added to a coated FACS collection tube just before FACS
419 flow started. The pre-sorted tube was controlled at 4˚C, and the collection tube was controlled
420 at 5˚C. Fluorescence-Activated BD Aria Fusion with a 130nm nozzle and 10 PSI pressure was
421 used for cell sorting. Auto-fluorescence typically peaks between approximately 380 and 600nm
422 (ultraviolet to red light). Therefore, a combination of five laser fluorescent detectors was
423 utilised to maximise yield. The auto-fluorescent cell population was sorted first by cells that
424 were auto-fluorescent, then by area, and lastly by width.

425 *scRNA-Seq Sequencing*

426 Following FACS, the final cell suspension was centrifuged at 500 x g for 10 mins. All liquid
427 was discarded from the top, leaving 30µl (max volume able to be inserted into the 10x
428 Genomics microfluidic chip). The remaining sample was loaded on the 10x Chromium
429 controller for scRNA-Seq conducted in accordance with the protocols established by 10x
430 Genomics - Universal 3' Gene Expression (Chromium Next GEM Single Cell 3′ Kit v3.1, 4
431 rxns PN-1000269).

432 scRNA-Seq was conducted by the Genomic Core Facility and the Bioinformatics Support Unit
433 at Newcastle University, achieving a sequencing depth of 50,000 reads per cell through
434 Illumina NovaSeq 6000. The binary base call (BCL) files underwent de-multiplexing through
435 CellRanger mkfastq version 3.01 to create FASTQ files, followed by alignment and
436 quantification against the human reference genome GRCh38 utilising CellRanger count.
437 Quality control assessments were conducted for each sample in R, eliminating any cells with
438 fewer than 1000 reads, fewer than 500 genes, or more than 10% mitochondrial reads.
439 Additionally, cells expressing haemoglobin genes were excluded from the analysis. The
440 identification of doublets was performed using DoubletFinder, and these were subsequently
441 filtered out from the dataset. Seurat (version 4.3.0) was then used to carry out normalisation in
442 order to eliminate intercellular variations, address discrepancies in gene expression, identify
443 2000 biologically significant variable genes, and perform data reduction using principal
444 component analysis (PCA) and clustering. The scaling process involved analysing factors:

445 “nFeature_RNA”, “percent.mt”, and “nCount_RNA”. PCA was conducted on the scaled data
446 utilising the FindPCA function, focusing on the 2000 genes identified as having the highest
447 variability.

448 Retinal cells were subsequently extracted from the individual samples, and batch effects were
449 mitigated using Harmony (version 0.1.1) to generate a unified dataset. The data visualisation
450 was performed through Uniform Manifold Approximation and Projection (UMAP).

451 *Cluster Analysis*

452 Qiagen Ingenuity Pathway Analysis (IPA) software was used for in-depth examination of the
453 differentially expressed gene lists derived from RNA sequencing via IPA core analysis. IPA
454 synthesises meticulously curated information from a variety of biological data sources,
455 including gene expression, molecular interactions, and pathway data from a vast experimental
456 database. This synthesis facilitates the identification of crucial biological signals. The outcomes
457 of the differential expression analysis were refined to retain only those with a p_val_adjust of
458 0.05 or lower for each cell type, subsequently uploaded to IPA. The gene symbols were
459 designated as ID with the selection of the 'Gene symbol' option. The avg_log2FC and p_val_adj
460 were utilised as the 'Observations', with 'Exprs Fold Change' and 'Exprs False Discovery Rate'
461 options applied respectively. Next, the core analysis was conducted by selecting the 'Expression
462 Analysis' option, with 'Exprs Fold Change' chosen to compute the z-score. This analysis was
463 performed utilising the 'Ingenuity knowledge base (genes only)', taking into account both
464 'Direct and indirect' relationships, and 'Causal networks' were selected. Following the
465 completion of the core analysis, the 'Upstream regulators' option was selected, and the results
466 were organised by z-score to identify the networks exhibiting the highest activation scores.

467

468 **Electrophysiology Methods**

469 Retinas were isolated from mouse pups at P2 (N=4 retinas), P3 (N=4), P4 (N=10), P5 (N=14),
470 P6 (N=3), P7 (N=2), P8 (N=2), P9 (N=2), P10 (N=2), P11 (N=2), P12 (N=1), P13 (N=1). The
471 isolated retina was placed, RGC layer facing down, onto the MEA and maintained stable by
472 placing a small piece of polyester membrane filter (Sterlitech, Kent, WA, USA) on the retina
473 followed by a bespoke anchor. The retina was kept in constant darkness at 32°C with an in-line
474 heater (Warner Instruments, Hamden, CT, USA) and continuously perfused using a peristaltic
475 pump (~1 ml/min) with artificial cerebrospinal fluid equilibrated with 95% $O_2$ and 5% $CO_2$.
476 Retinas rested in-situ for 2 hours before recording, allowing sufficient time for spontaneous
477 activity to reach steady-state levels. Probenecid (4-(dipropylsulfamoyl)benzoic acid) (water
478 soluble form, ThermoFisher Scientific, P36400) was used at 1mM.

479 High density MEA extracellular recordings of spontaneous waves were performed as described
480 in detail in Maccione et al. (2014), using the BioCam4096 platform with APS MEA chips type
481 HD-MEA Stimulo (3Brain GmbH, Switzerland), providing 4096 square microelectrodes of 21
482 µm x 21 µm in size on an active area of 5.12 x 5.12 $mm^2$, with an electrode pitch of 81 µm.
483 Two P5 and one P4 datasets were acquired with the MEA chip HD-MEA Arena (2.67x2.67$mm^2$
484 active area, electrode pitch 42 µm) for electrical imaging.

485 Raw signals were visualised and recorded at 7 kHz sampling rate with BrainWaveX (3Brain
486 GmbH, Switzerland). Each dataset consisted of 30 minutes of continuous recording of retinal
487 waves. Following the recording session, retinas were photographed on the MEA to document
488 their precise orientation relative to the electrode array.

489

490 **Calcium Imaging Methods**

491 *Tissue Preparation*

492 C57BL/6 pups from P3 (N=8), P4 (N=15), P5 (N=11), and P6 (N=8) were enucleated, and
493 retinas were dissected at room temperature in oxygenated ACSF under a dissecting microscope.
494 Isolated retinas were mounted whole onto a hydrophilic PTFE membrane (H100A047A
495 Advantec, Japan) with the retinal ganglion cell layer facing upwards. All further incubations
496 were conducted at 35C° in a hyperoxygenated darkened chamber. P4 and older retinas
497 underwent incubation in 0.0001% Pronase E (P5147 Sigma-Aldrich) for 30 minutes to
498 permeabilise the inner limiting membrane (ILM) (Dalkara et al., 2009). To label the extent of
499 vascularisation, the retinas were incubated in isolectin B4 594 (DL-1208, Vector Labs) for 30
500 minutes at 10 µg/ml (Stucky & Lewin, 1999). Retinas were bath loaded with the calcium
501 indicator Cal 520 AM (AAT Bioquest) (10µM) for 2 hours and were then flattened further with
502 a second piece of PTFE membrane placed on top and before transferring to the imaging
503 microscope. The retinas were perfused with fresh oxygenated aCSF with a peristaltic pump at
504 1.7 ml/min. Tissue was allowed to settle in the perfused heated solution for at least 30 minutes
505 before imaging.

506 *Data Acquisition*

507 Imaging was conducted in the Newcastle University Functional and Light-Activatable Multi-
508 dimensional Electrophysiology facility (FLAME). This was conducted on a Nikon FN1
509 microscope at x4 NA 0.2 (Nikon CFI Plan Apochromat Lambda D 4X) magnification with a
510 x0.63 relay lens resulting in a field of view of 5.3x 5.3 mm and a resolution of 2.6µm per pixel.
511 To enable multiple wavelength imaging the microscope used a quad band Chroma 89402 filter
512 cube. Images were acquired at 470nm and 590nm for the calcium signal and blood vessels
513 respectively. Time series images were acquired at 2Hz for 10 minutes at 2048 x 2048 pixels at
514 16bit resolution. For drug applications, an appropriate wash in and wash out time was used
515 according to the literature. Probenecid (1mM) was used to block purinergic release from
516 apoptotic cells and examine the effect on retinal wave generation/spread.

517 *Data Processing and Analysis*

518 All data processing was conducted in MATLAB. Image time series were motion corrected
519 using 2D cross-correlation approach. To properly visualise the retinal waves the time series
520 were downsampled to 512 x 512 pixels and went through a pixel-wise ΔF/F procedure. The
521 calcium activity baseline was calculated by creating a low-pass percentage filtered trace. Each
522 movie frame (F) was normalized by dividing its difference from the baseline frame (F- F0) by
523 the baseline frame ((F- F0)/F0) to produce a ΔF/F movie.

To track the spatiotemporal properties of the calcium waves the ΔF/F movies were thresholded, and the waves were identified with a semi-automated algorithm to determine their identity. Once this was done, a large variety of metrics were extracted including initiation point, speed, area, frequency, and spatial relation to vascularised area.

All code relating to this project can be found here: https://github.com/GrimmSnark/paperCodeSavage2026

**Immunohistochemistry**

*Immunostaining*

Whole-mount retinas were prepared from mouse pups aged P2-P11, flattened on nitrocellulose membrane filters or PTFE membrane and fixed for 45 min in 4% PFA. Some retinas were labelled for apoptotic cells with the selective YO-PRO-1 dye (Y3603, Invitrogen) at 200uM for 1 hour in carbogenated aCSF before fixation. Retinas were incubated with the primary antibodies (RBPMS 1830-RBPMS, rabbit polyclonal, Phosphosolutions (1:500), ChAT AB144P, goat polyclonal, Merck Millipore (1:500),VChAT PA5-77386, rabbit polyclonal, ThermoFisher Scientific) (1:500), Iba-1 019-19741, rabbit polyclonal, Alpha Labs (1:1000), HMOX-1 AB_2118685, rabbit polyclonal, Proteintech (1:1000), PANX-1 488100, rabbit polyclonal, Invitrogen (1:500)) with 0.5% Triton X-100 in PBS for 3 days at 4°C, then washed with PBS and incubated with the secondary antibody solution for 1 day at 4°C (with or without IB4). Secondary antibodies included 0.5% Triton X-100 with donkey anti rabbit Alexa 568 (1:500), donkey anti-goat Dylight 488 (1:500), goat anti-rabbit A546 (1:500). Isolectin B4 (IB4) staining of blood vessels (1:250) was performed together with the secondary antibody staining step. Finally, retinas were washed with PBS and embedded with Vectashield (H-1900, Vector Laboratories).

For a specific antibody lot of PANX-1, the tissue underwent an additional antigen retrieval step in a water bath at 80°C for 30 minutes using sodium citrate. Retinas were then incubated in blocking solution (5% secondary antibody host species serum with 0.5% Triton X-100 in PBS) for 1 hour.

*Imaging*

Zeiss AxioImager with Apotome and a Zeiss LSM 800 confocal microscope were used to image the retinas. High-resolution images of the RGC layer down to the inner nuclear layer (INL) were obtained by subdividing retinal wholemounts into adjacent smaller images that were subsequently stitched back together to view the entire retinal surface. Regions of interest were selected around the clusters.

To compensate for variability in retinal thickness, several focus points were set across the retinal surface to maintain sharp focus on the desired cell layer. Each picture was then acquired in all colour channels at 20x magnification, and with 10% overlap between neighbouring areas. This overlap is used to correctly align and stitch together all pictures using the Zen Pro software (Zeiss). Some wide-field fluorescent images were acquired with the Nikon Ni-E microscope. Grids of 5x5-8x8 images were taken at 10x or 20x, and then combined to obtain a high-resolution image of the whole retina

564 *Peripherality and Vascular Relation Metrics (D1/2, and D1/3)*

565 To determine the relative position of objects—including ACCs, labelled cells, and wave
566 origins, we calculated the distance from the optic nerve head to the object (D1) and through to
567 the retinal periphery (D2). The ratio (D1/D2) provides a measure of an object's relative
568 peripherality, independent of individual retinal size. Additionally, for a subset of samples, we
569 measured the distance from the optic nerve head through the object to the margin of the
570 superficial vascular plexus (D3). Accordingly, a ratio of D1/3 <= 1 defined an object within the
571 vascularised area, while D1/3> 1 was in the non-vascularised area indicated a position in the
572 non-vascularised region (see **Figure S2** for details).

573 For the ACC D1/2 values (Figure 1F) one-way ANOVA was used on all 233 ratio values for all
574 eight groups. Tukey post-hoc test was used to identify significant changes in cluster positions
575 between consecutive developmental days.

576 *Vascular Plexus Analysis*

577 Sholl analysis was performed using FIJI to quantify blood vessel branches. IB4 stained
578 vasculature images from retinal wholemounts were rendered binary using the 'Threshold'
579 function. To remove signals inherent to auto-fluorescence of the ACCs, a separate colour
580 channel image showing only cluster cells was rendered binary and subtracted from the
581 vasculature image. Subtracted images were then adjusted using the 'Brightness/Contrast'
582 function to obtain solid binary images.

583 To quantify blood vessel density in the vicinity of ACCs, segmental sections of the binary,
584 cluster-subtracted whole retina vasculature images were outlined using the 'Angle' tool
585 (allowing measurement of the angle of the segment and subsequent calculation of the surface
586 area of the region of interest (ROI)) either with or without a cluster at the edge of the vascular
587 plexus. Sholl rings were set from the centre of the ONH with a step size of 30 µm.
588 Measurements were not taken from the inner 50 % of the segment (based on the radius of the
589 vascular plexus at its largest point). Intersections were counted manually.

590 To quantify blood vessel branch density in areas with ACCs versus areas without at matching
591 eccentricities, ROIs were outlined using the 'Polygons' function either around clusters (ACC+
592 ROI), or in adjacent ACC negative regions at similar eccentricities (ACC- ROI). This was done
593 in images from a colour channel in which the blood vessels were not visible. Once all ROIs
594 were outlined for one retina, they were overlaid on the binary, cluster subtracted vasculature
595 image for that same retina. Any ROIs noticeably outside of the vascular plexus were
596 discounted. Sholl rings were set from the centre of the ONH with a step size of 30 µm.
597 Intersections were counted manually.

598 All cell counts were performed using FIJI. Cluster cells were counted manually in retinal
599 wholemount images using the 'Multi-point' function. Cells were identified by auto-
600 fluorescence using an image captured on a channel without any fluorescing immunostaining.
601 The vascular plexus was outlined using the 'Freehand' tool and 'Measure' function was used
602 to determine surface area. Clusters were delimited and cells counted manually, identified by
603 auto-fluorescence. A 'cluster' was defined as an uninterrupted group of auto-fluorescent cells

spatially separated from any other group, localised near the outer edge of the superficial vascular plexus. No lower or upper size limit was assigned to clusters.

*ACCs and Microglial Densities*

To quantify microglia and ACC densities, radial straight lines were drawn from the centre of the ONH to the periphery of the retina, either through the centre of an ACC group or through an adjacent ACC negative region. This was only performed where radial lines reached the periphery of the retina, uninterrupted by cuts. ROIs were outlined using the 'Oval' selection tool at four points along each radial line to comprise an ROI set. The four ROI types in each set were ahead of the ACC positive/negative region, at the ACC positive/negative region, behind the ACC positive/negative region, and close to the ONH. ROIs were outlined at comparable eccentricities for each set. Iba1 stained microglia were counted manually. All Iba1 stained whole retinas were from P5 or P6 animals. ACCs were identified by auto-fluorescence and counted manually.

*Quantification of microglia, apoptotic cells and co-localisation*

For retinal wholemounts stained for HMOX-1 and YO-PRO-1 binary masks were created with FIJI/ImageJ, Labkit (Arzt, M. et al 2022), and custom MATLAB code. Labelled cells were counted and co-localisation percentages were also calculated. This was based on the HMOX-1 microglia mask containing any positively labelled pixels from the YO-PRO-1 channel. Statistical testing between different drug conditions was conducted with a Kruskal-Wallis ANOVA test with multiple comparisons, threshold at $p= 0.05$.

**Microglia Morphometry**

*Computational Microglia Labelling*

Images were processed and filtered using FIJI/ImageJ (Schindelin et al., 2012). Images were cleaned for background noise using Gaussian convoluted background subtraction ($\sigma = 50$ pixels) and median filtering (3 x 3 pixels). Single colour image channels depicting stained cells of interest (YO-PRO-1, Hmox1 etc) were segmented with Labkit (Arzt, M. et al 2022) and custom code (https://github.com/GrimmSnark/paperCodeSavage2026). Quantitative measurements of the labelled microglia were conducted utilising the FIJI plugin "Measure Microglia Morphometry" (Martinez et al. 2023). Briefly, this plugin quantifies a plethora of morphological metrics including area, perimeter, convex area, average branch length, and branch point number (Figure S1.)

*Microglial Behavioural Parameters Statistical Analysis*

Statistical analysis and data visualisation were performed using GraphPad Prism 10. Two-tailed Mann-Whitney tests and non-parametric ANOVA were applied, with a significance threshold set at $P \leq 0.05$. Given the non-parametric nature of the data distribution, results were presented as the median accompanied by a 95% Confidence Interval (CI). The significance levels are indicated as follows: not significant (ns) for $P > 0.05$, * for $P \leq 0.05$, ** for $P \leq 0.01$, *** for $P \leq 0.001$, and **** for $P \leq 0.0001$.

**Acknowledgements:** We are grateful to Leverhulme Trust (RPG-2022-061), BBSRC (BB/T017627/1) and EPSRC/ERC (EP/Y031016/1) for funding this work. We would also like to thank the Newcastle University FMS Bioimaging Unit for their continual support during this project.

This work is dedicated to the memory of Evelyne Sernagor, who conceptualised and led this study until her passing in March 2025. Her brilliance and mentorship remain the foundation of this research.

Authour contributions (CRediT):

**Michael A. Savage:** Conceptualization, Methodology, Software, Validation, Formal analysis, Investigation, Data Curation, Writing - Original Draft, Visualization, Project administration

**Cori Bertram:** Methodology, Validation, Formal analysis, Investigation, Data Curation, Visualization

**Jean de Montigny:** Conceptualization, Software, Formal analysis, Investigation, Data Curation, Visualization

**Courtney A. Thorne:** Investigation, Formal analysis, Visualization

**Rachel Queen:** Software, Formal analysis, Visualization

**Majlinda Lako:** Conceptualization, Methodology, Resources, Supervision, Writing - Review & Editing, Project administration, Funding acquisition

**Gerrit Hilgen:** Writing - Review & Editing, Supervision

**Evelyne Sernagor:** Conceptualization, Methodology, Formal analysis, Investigation, Resources, Writing - Original Draft, Supervision, Project administration, Funding acquisition

## References

Ackman, J. B., Burbridge, T. J., & Crair, M. C. (2012). Retinal waves coordinate patterned activity throughout the developing visual system. *Nature*, *490*(7419), 219–225. https://doi.org/10.1038/nature11529

Anderson, S. R., Roberts, J. M., Zhang, J., Steele, M. R., Romero, C. O., Bosco, A., & Vetter, M. L. (2019). Developmental Apoptosis Promotes a Disease-Related Gene Signature and Independence from CSF1R Signaling in Retinal Microglia. *Cell Reports*, *27*(7), 2002-2013.e5. https://doi.org/10.1016/j.celrep.2019.04.062

Babola, T. A., Li, S., Wang, Z., Kersbergen, C. J., Elgoyhen, A. B., Coate, T. M., & Bergles, D. E. (2021). Purinergic signaling controls spontaneous activity in the auditory system throughout early development. *Journal of Neuroscience*, *41*(4), 594–612. https://doi.org/10.1523/JNEUROSCI.2178-20.2020

Bansal, A., Singer, J. H., Hwang, B. J., Xu, W., Beaudet, A., & Feller, M. B. (2000). Mice Lacking Specific Nicotinic Acetylcholine Receptor Subunits Exhibit Dramatically Altered Spontaneous Activity Patterns and Reveal a Limited Role for Retinal Waves in Forming ON and OFF Circuits in the Inner Retina. *Journal of Neuroscience*, *20*(20), 7672–7681. https://doi.org/10.1523/jneurosci.20-20-07672.2000

Bao, L., Locovei, S., & Dahl, G. (2004). Pannexin membrane channels are mechanosensitive conduits for ATP. *FEBS Letters*, *572*(1–3), 65–68. https://doi.org/10.1016/j.febslet.2004.07.009

Blankenship, A. G., & Feller, M. B. (2010). Mechanisms underlying spontaneous patterned activity in developing neural circuits. In *Nature Reviews Neuroscience* (Vol. 11, Issue 1, pp. 18–29). Nature Publishing Group. https://doi.org/10.1038/nrn2759

Blankenship, A. G., Ford, K. J., Johnson, J., Seal, R. P., Edwards, R. H., Copenhagen, D. R., & Feller, M. B. (2009). Synaptic and Extrasynaptic Factors Governing Glutamatergic Retinal Waves. *Neuron*, *62*(2), 230–241. https://doi.org/10.1016/j.neuron.2009.03.015

Catsicas, M., Bonness, V., Becker, D., & Mobbs, P. (1998). Spontaneous Ca2+ transients and their transmission in the developing chick retina. *Current Biology*, *8*(5), 283–288. https://doi.org/10.1016/s0960-9822(98)70110-1

Chan-Ling, T., Gock, B., & Stone, J. (1995). The effect of oxygen on vasoformative cell division: Evidence that "physiological hypoxia" is the stimulus for normal retinal vasculogenesis. *Investigative Ophthalmology and Visual Science*, *36*(7), 1201–1214.

Checchin, D., Sennlaub, F., Levavasseur, E., Leduc, M., & Chemtob, S. (2006). Potential Role of Microglia in Retinal Blood Vessel Formation. *Investigative Ophthalmology & Visual Science*, *47*(8), 3595–3602. https://doi.org/10.1167/IOVS.05-1522

Chen, V. S., Morrison, J. P., Southwell, M. F., Foley, J. F., Bolon, B., & Elmore, S. A. (2017). Histology Atlas of the Developing Prenatal and Postnatal Mouse Central Nervous System, with Emphasis on Prenatal Days E7.5 to E18.5. *Toxicologic Pathology*, *45*(6), 705–744. https://doi.org/10.1177/0192623317728134

Cornell, J., Salinas, S., Huang, H. Y., & Zhou, M. (2022). Microglia regulation of synaptic plasticity and learning and memory. In *Neural Regeneration Research* (Vol. 17, Issue 4, pp. 705–716). Wolters Kluwer Medknow Publications. https://doi.org/10.4103/1673-5374.322423

Dvoriantchikova, G., Ivanov, D., Panchin, Y., & Shestopalov, V. I. (2006). Expression of pannexin family of proteins in the retina. *FEBS Letters*, *580*(9), 2178–2182. https://doi.org/10.1016/j.febslet.2006.03.026

Edlich, F., Banerjee, S., Suzuki, M., Cleland, M. M., Arnoult, D., Wang, C., Neutzner, A., Tjandra, N., & Youle, R. J. (2011). Bcl-xL retrotranslocates Bax from the mitochondria into the cytosol. *Cell*, *145*(1), 104–116. https://doi.org/10.1016/j.cell.2011.02.034

Farah, M. H., & Easter, S. S. (2005). Cell birth and death in the mouse retinal ganglion cell layer. *Journal of Comparative Neurology*, *489*(1), 120–134. https://doi.org/10.1002/CNE.20615;PAGE:STRING:ARTICLE/CHAPTER

Feller, M. B., Wellis, D. P., Stellwagen, D., Werblin, F. S., & Shatz, C. J. (1996). Requirement for Cholinergic Synaptic Transmission in the Propagation of Spontaneous Retinal Waves. *Science*, *272*(5265), 1182–1187. https://doi.org/10.1126/science.272.5265.1182

Firth, S. I., Wang, C. T., & Feller, M. B. (2005). Retinal waves: Mechanisms and function in visual system development. In *Cell Calcium* (Vol. 37, Issue 5 SPEC. ISS., pp. 425–432). Churchill Livingstone. https://doi.org/10.1016/j.ceca.2005.01.010

Fontainhas, A. M., Wang, M., Liang, K. J., Chen, S., Mettu, P., Damani, M., Fariss, R. N., Li, W., & Wong, W. T. (2011). Microglial morphology and dynamic behavior is regulated by ionotropic glutamatergic and GABAergic neurotransmission. *PLoS ONE*, *6*(1). https://doi.org/10.1371/journal.pone.0015973

Gao, J., Li, B., Tian, H., Li, C., Merzlikin, N., Han, D., Ling, Z., Zhang, Z., Zhu, W., Dai, J., Gerunova, L., Lv, C., Li, N., & Hua, J. (2025). SPARC-modified mesenchymal stem cells promote recovery of β-cells and insulin secretion by calcium ion homeostasis. *Stem Cell Research and Therapy*, *16*(1), 607-. https://doi.org/10.1186/s13287-025-04727-2

Gariano, R. F., & Gardner, T. W. (2005). Retinal angiogenesis in development and disease. In *Nature* (Vol. 438, Issue 7070, pp. 960–966). Nature. https://doi.org/10.1038/nature04482

Gupta, A., Rarick, K. R., & Ramchandran, R. (2021). Established, New and Emerging Concepts in Brain Vascular Development. In *Frontiers in Physiology* (Vol. 12, p. 636736). Frontiers Media S.A. https://doi.org/10.3389/fphys.2021.636736

Han, J. W., Flemington, C., Houghton, A. B., Gu, Z., Zambetti, G. P., Lutz, R. J., Zhu, L., & Chittenden, T. (2001). Expression of bbc3, a pro-apoptotic BH3-only gene, is regulated by diverse cell death and survival signals. *Proceedings of the National Academy of Sciences of the United States of America*, *98*(20), 11318–11323. https://doi.org/10.1073/pnas.201208798

Imamura, Y., Noda, S., Hashizume, K., Shinoda, K., Yamaguchi, M., Uchiyama, S., Shimizu, T., Mizushima, Y., Shirasawa, T., & Tsubota, K. (2006). Drusen, choroidal neovascularization, and retinal pigment epithelium dysfunction in SOD1-deficient mice: A model of age-related macular degeneration. *Proceedings of the National Academy of Sciences of the United States of America*, *103*(30), 11282–11287. https://doi.org/10.1073/pnas.0602131103

Kennedy, C. J., Rakoczy, P. E., & Constable, I. J. (1995). Lipofuscin of the retinal pigment epithelium: A review. *Eye (Basingstoke)*, *9*(6), 763–771. https://doi.org/10.1038/eye.1995.192

Koso, H., Tsuhako, A., Lai, C. Y., Baba, Y., Otsu, M., Ueno, K., Nagasaki, M., Suzuki, Y., & Watanabe, S. (2016). Conditional rod photoreceptor ablation reveals Sall1 as a microglial marker and regulator of microglial morphology in the retina. *GLIA*, *64*(11), 2005–2024. https://doi.org/10.1002/glia.23038

Kuan, C. Y., Roth, K. A., Flavell, R. A., & Rakic, P. (2000). Mechanisms of programmed cell death in the developing brain. In *Trends in Neurosciences* (Vol. 23, Issue 7, pp. 291–297). Trends Neurosci. https://doi.org/10.1016/S0166-2236(00)01581-2

Liu, Y., Tang, J., Wei, P., Yu, Z., Wu, Z., Zhao, X., Qi, H., Liu, P., Zheng, M., Mi, S., Du, W., Vavvas, D. G., Cui, K., & Zhang, G. (2026). Microglial HMOX1 drives retinal angiogenesis via modulation of endothelial STAT3 signaling. *Free Radical Biology and Medicine*, *243*, 29–42. https://doi.org/10.1016/J.FREERADBIOMED.2025.11.018

Lou, N., Takano, T., Pei, Y., Xavier, A. L., Goldman, S. A., & Nedergaard, M. (2016). Purinergic receptor P2RY12-dependent microglial closure of the injured blood-brain barrier. *Proceedings of the National Academy of Sciences of the United States of America*, *113*(4), 1074–1079. https://doi.org/10.1073/pnas.1520398113

Maccione, A., Hennig, M. H., Gandolfo, M., Muthmann, O., van Coppenhagen, J., Eglen, S. J., Berdondini, L., & Sernagor, E. (2014). Following the ontogeny of retinal waves: Pan-retinal recordings of population dynamics in the neonatal mouse. *Journal of Physiology*, *592*(7), 1545–1563. https://doi.org/10.1113/jphysiol.2013.262840

Martineau, S., Valdez-Lopez, J. C., Zarnick, S., & Kay, J. N. (2026). Microglia and Myeloid Cell Populations of the Developing Mouse Retina. *GLIA*, *74*(2), e70115. https://doi.org/10.1002/glia.70115

Nakao, T., Ishizawa, A., & Ogawa, R. (1988). Observations of vascularization in the spinal cord of mouse embryos, With special reference to development of boundary membranes and perivascular spaces. *The Anatomical Record*, *221*(2), 663–677. https://doi.org/10.1002/ar.1092210212

O'Donovan, M. J. (1999). The origin of spontaneous activity in developing networks of the vertebrate nervous system. *Current Opinion in Neurobiology*, *9*(1), 94–104. https://doi.org/10.1016/S0959-4388(99)80012-9

Ohsawa, K., Imai, Y., Kanazawa, H., Sasaki, Y., & Kohsaka, S. (2000). Involvement of Iba1 in membrane ruffling and phagocytosis of macrophages/microglia. *Journal of Cell Science*, *113*(17), 3073–3084. https://doi.org/10.1242/jcs.113.17.3073

Paredes, I., Himmels, P., & Ruiz de Almodóvar, C. (2018). Neurovascular Communication during CNS Development. In *Developmental Cell* (Vol. 45, Issue 1, pp. 10–32). Cell Press. https://doi.org/10.1016/j.devcel.2018.01.023

Rodriguez, A. R., de Sevilla Müller, L. P., & Brecha, N. C. (2014). The RNA binding protein RBPMS is a selective marker of ganglion cells in the mammalian retina. *Journal of Comparative Neurology*, *522*(6), 1411–1443. https://doi.org/10.1002/cne.23521

775 Sernagor, E., Eglen, S. J., & O'Donovan, M. J. (2000). Differential effects of acetylcholine and glutamate
776 blockade on the spatiotemporal dynamics of retinal waves. *The Journal of Neuroscience : The Official*
777 *Journal of the Society for Neuroscience*, *20*(2). https://doi.org/10.1523/jneurosci.20-02-j0004.2000

778 Sernagor, E., & Grzywacz, N. M. (1996). Influence of spontaneous activity and visual experience on developing
779 retinal receptive fields. *Current Biology*, *6*(11), 1503–1508. https://doi.org/10.1016/S0960-
780 9822(96)00755-5

781 Sernagor, E., & Grzywacz, N. M. (1999). Spontaneous activity in developing turtle retinal ganglion cells:
782 Pharmacological studies. *Journal of Neuroscience*, *19*(10), 3874–3887.
783 https://doi.org/10.1523/jneurosci.19-10-03874.1999

784 Sernagor, E., Young, C., & Eglen, S. J. (2003). Developmental Modulation of Retinal Wave Dynamics:
785 Shedding Light on the GABA Saga. *The Journal of Neuroscience*, *23*(20), 7621.
786 https://doi.org/10.1523/JNEUROSCI.23-20-07621.2003

787 Spaide, R. F., & Curcio, C. A. (2010). Drusen characterization with multimodal imaging. *Retina*, *30*(9), 1441–
788 1454. https://doi.org/10.1097/IAE.0b013e3181ee5ce8

789 Sparrow, J. R. (2007). Lipofuscin of the retinal pigment epithelium. In *Atlas of Fundus Autofluorescence*
790 *Imaging* (pp. 3–16). Springer, Berlin, Heidelberg. https://doi.org/10.1007/978-3-540-71994-6_1

791 Stafford, B. K., Sher, A., Litke, A. M., & Feldheim, D. A. (2009). Spatial-Temporal Patterns of Retinal Waves
792 Underlying Activity-Dependent Refinement of Retinofugal Projections. *Neuron*, *64*(2), 200–212.
793 https://doi.org/10.1016/j.neuron.2009.09.021

794 Stellwagen, D., Shatz, C. J., & Fellert, M. B. (1999). Dynamics of retinal waves are controlled by cyclic AMP.
795 *Neuron*, *24*(3), 673–685. https://doi.org/10.1016/S0896-6273(00)81121-6

796 Stevens, B., Allen, N. J., Vazquez, L. E., Howell, G. R., Christopherson, K. S., Nouri, N., Micheva, K. D.,
797 Mehalow, A. K., Huberman, A. D., Stafford, B., Sher, A., Litke, A. M. M., Lambris, J. D., Smith, S. J.,
798 John, S. W. M., & Barres, B. A. (2007). The Classical Complement Cascade Mediates CNS Synapse
799 Elimination. *Cell*, *131*(6), 1164–1178. https://doi.org/10.1016/j.cell.2007.10.036

800 Stillman, J. M., Mendes Lopes, F., Lin, J. P., Hu, K., Reich, D. S., & Schafer, D. P. (2023). Lipofuscin-like
801 autofluorescence within microglia and its impact on studying microglial engulfment. *Nature*
802 *Communications*, *14*(1), 7060-. https://doi.org/10.1038/s41467-023-42809-y

803 Syed, M. M., Lee, S., He, S., & Zhou, Z. J. (2004). Spontaneous Waves in the Ventricular Zone of Developing
804 Mammalian Retina. *Journal of Neurophysiology*, *91*(5), 1999–2009.
805 https://doi.org/10.1152/jn.01129.2003

806 Syed, M. M., Lee, S., Zheng, J., & Zhou, Z. J. (2004). Stage-dependent dynamics and modulation of
807 spontaneous waves in the developing rabbit retina. *Journal of Physiology*, *560*(2), 533–549.
808 https://doi.org/10.1113/jphysiol.2004.066597

809 Velasquez, S., & Eugenin, E. A. (2014). Role of Pannexin-1 hemichannels and purinergic receptors in the
810 pathogenesis of human diseases. In *Frontiers in Physiology: Vol. 5 MAR*. Front Physiol.
811 https://doi.org/10.3389/fphys.2014.00096

812 Weiner, G. A., Shah, S. H., Angelopoulos, C. M., Bartakova, A. B., Pulido, R. S., Murphy, A., Nudleman, E.,
813 Daneman, R., & Goldberg, J. L. (2019). Cholinergic neural activity directs retinal layer-specific
814 angiogenesis and blood retinal barrier formation. *Nature Communications*, *10*(1), 2477-.
815 https://doi.org/10.1038/s41467-019-10219-8

816 Wong, W. T., Sanes, J. R., & Wong, R. O. L. (1998). Developmentally regulated spontaneous activity in the
817 embryonic chick retina. *Journal of Neuroscience*, *18*(21), 8839–8852.
818 https://doi.org/10.1523/jneurosci.18-21-08839.1998

819 Yamamoto, Y., & Henderson, C. E. (1999). Patterns of programmed cell death in populations of developing
820 spinal motoneurons in chicken, mouse, and rat. *Developmental Biology*, *214*(1), 60–71.
821 https://doi.org/10.1006/dbio.1999.9413

Zheng, J., Lee, S., & Zhou, Z. J. (2006). A transient network of intrinsically bursting starburst cells underlies the generation of retinal waves. *Nature Neuroscience*, *9*(3), 363–371. https://doi.org/10.1038/nn1644

Zhou, Z. J., & Zhao, D. (2000). Coordinated transitions in neurotransmitter systems for the initiation and propagation of spontaneous retinal waves. *Journal of Neuroscience*, *20*(17), 6570–6577. https://doi.org/10.1523/jneurosci.20-17-06570.2000

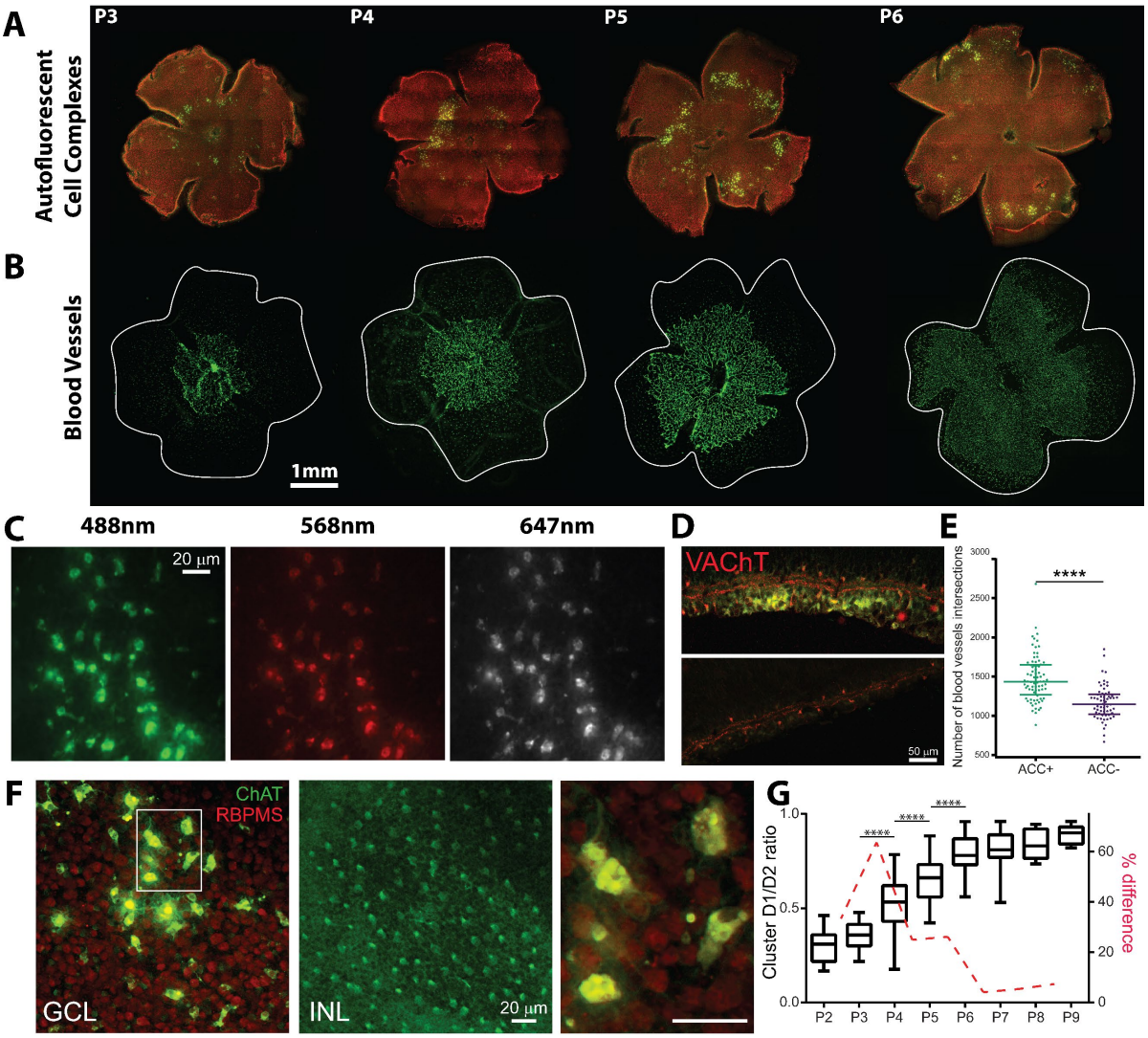


Figure 1: Auto-fluorescent Cluster Complexes (ACCs) display centrifugal development pattern during the first postnatal week in C57/BL6 and align with vasculature development. **A.** Mouse retinal wholemounts displaying ACCs (green) across P3-P6. **B.** Mouse retinal wholemounts (P3-P6) displaying SVP (labelled with Isolectin B4 (IB4)). Scale bar is equal to 1mm. **C.** Zoom into one auto-fluorescent cluster complex (P5) visualised at three different wavelengths without any additional immunolabeling, indicating intrinsic auto-fluorescent signals. **D.** Retinal sections showing VAChT (red) expression in a cluster area (upper panel, P4 retina) and in an area devoid of clusters (lower panel, P5 retina). **E.** Scatter plot of blood vessel branch intersections (Sholl analysis). There are significantly more branches in ACC positive areas (ACC +, green) than in ACC negative areas (ACC -, purple). Median with interquartile range. **F.** P5 cluster viewed at the GCL level and at the inner nuclear layer (INL) level in a whole-mount. Green: ChAT; red: RBPMS. The cluster cells are visible only at the GCL level and are much larger than SACs or RGCs (in red). At the INL level, there are only SACs and no ACCs. Right side of panel is magnified version of box on left. **G.** Box plot showing developmental changes in ACCs D1/D2 ratios. Each box illustrates the median (horizontal line) and interquartile range, with minimum and maximum values (whiskers). Asterisks indicate significant changes between consecutive days (One-way ANOVA with post-hoc Tukey test). The red dotted line illustrates the percentage difference in values between consecutive days, showing peak difference between P3 and P4 and no further changes from P6 onwards. ****: P<0.0001, Mann Whitney 2-tailed test.

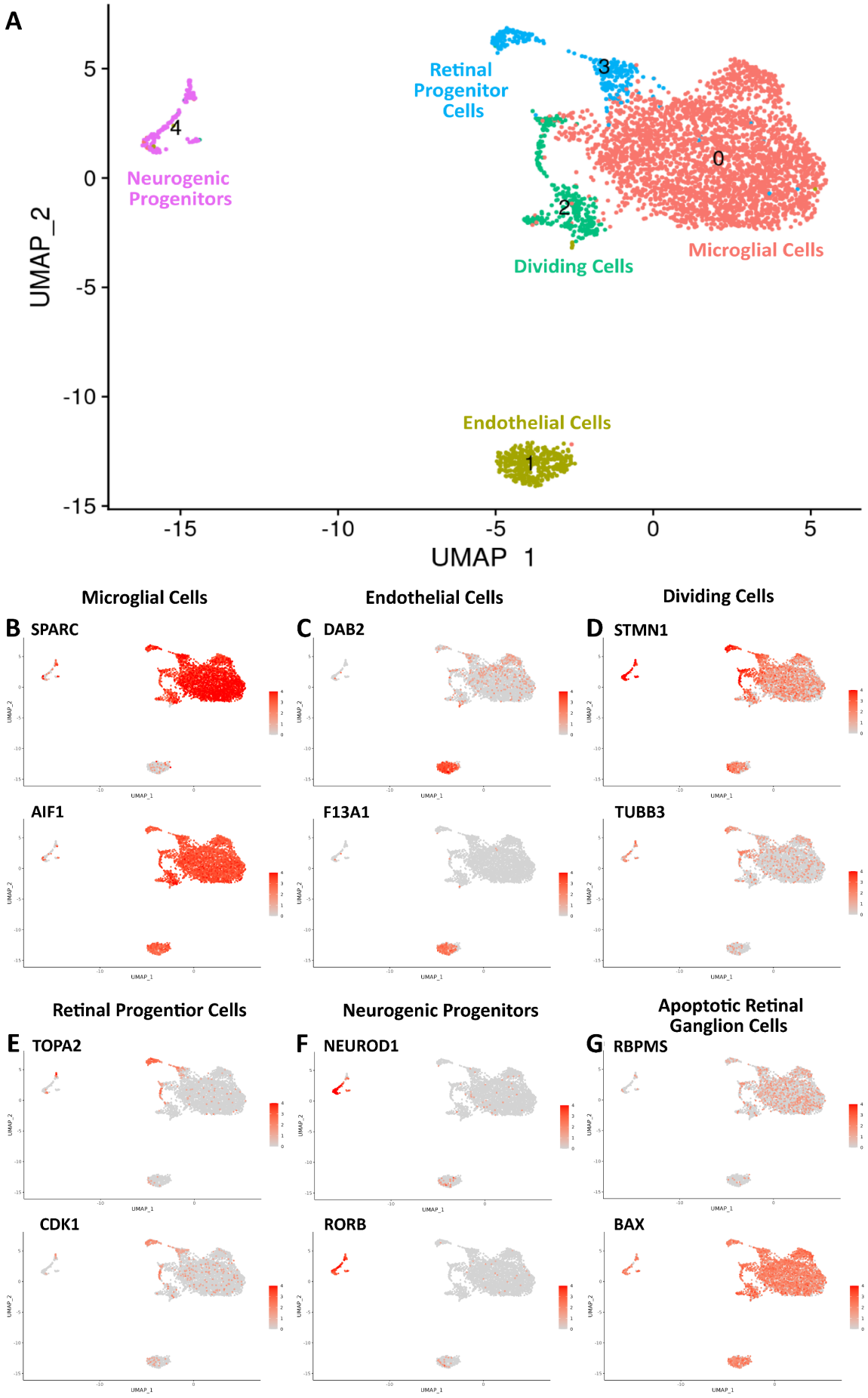
A
Retinal Progenitor Cells
Neurogenic Progenitors
Dividing Cells
Microglial Cells
Endothelial Cells
UMAP_2
UMAP_1
Microglial Cells
Endothelial Cells
Dividing Cells
B SPARC
C DAB2
D STMN1
AIF1
F13A1
TUBB3
Retinal Progentior Cells
Neurogenic Progenitors
Apoptotic Retinal Ganglion Cells
E TOPA2
F NEUROD1
G RBPMS
CDK1
RORB
BAX

848

*Figure 2: Genetic analysis of ACCs suggests they are complexes of microglia and dying RGCs.* **A.** UMAP plot of scRNA-Seq data derived from ACCs. Each cluster was identified based on the expression of retinal specific cell markers. Highly expressed markers for each cluster are shown in subsequent panels. **B.** Expression of microglia cell markers *SPARC* and *AIF1*. **C.** Expression of endothelial cell markers *DAB2* and *F13A1*. **D.** Expression of proliferating cell markers *STMN1* and *TUBB3*. **E.** Expression of RPC markers *TOPA2* and *CDK1*. **F.** Expression of neurogenic progenitor cell markers *NEUROD1* and *RORB*. **G.** Expression of retinal ganglion cell markers *RPBMS* and *BAX*.

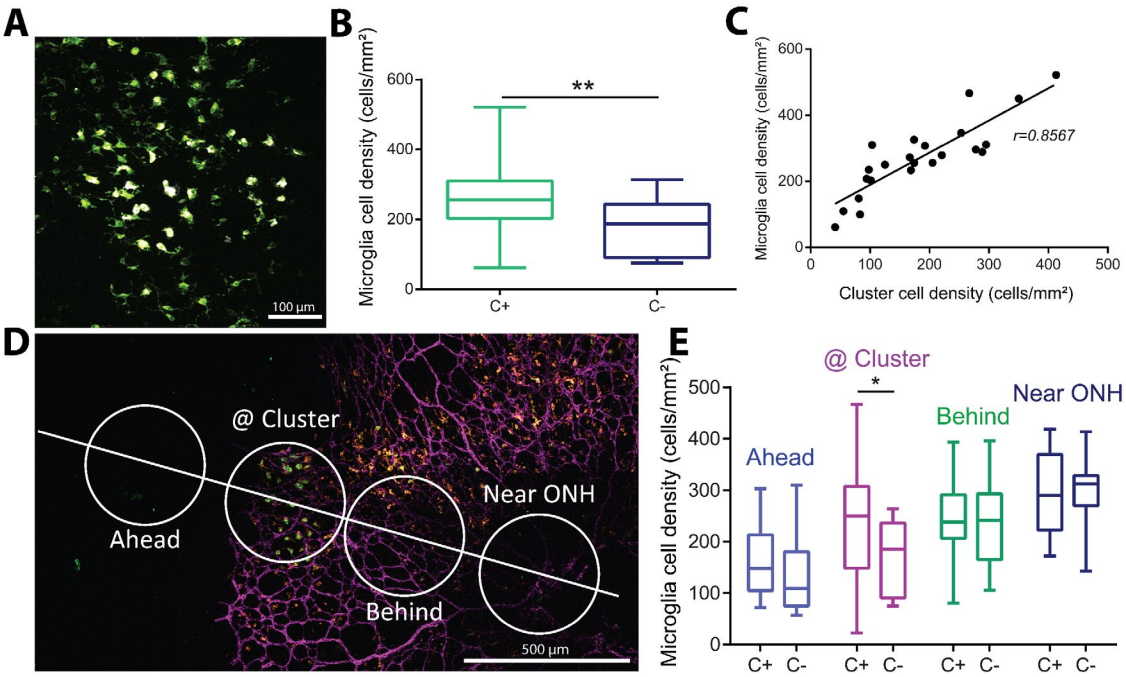


*Figure 3: Microglia associate with the ACCs* **A.** Representative micrograph of ACCs (white) surrounded by microglial cells labelled with iba1 (green) Scale = 100µm. **B.** Box plot (median and interquartile ranges) comparing microglia density within cluster areas (C+) versus cluster negative areas (C-). P<0.0138. Mann Whitney two-tailed test. **C.** Strong positive correlation between the densities of microglial cells and auto-fluorescent cluster cells (p<0.0001). **D.** Method for measuring microglia density at different retinal eccentricities, with measures taken near the ONH, between the ONH and clusters (behind) at clusters and ahead of clusters, further in the periphery, in the unvascularized part of the retina. The micrograph shows blood vessels lableled with IB4 (magenta), microglia labelled with iba1 (orange) and ACCs (white) Scale bar = 500µm. **E.** Box plot (with medians and interquartile ranges) showing that the density of microglia is significantly higher within clusters (p<0.01, Mann Whitney, two-tailed test).

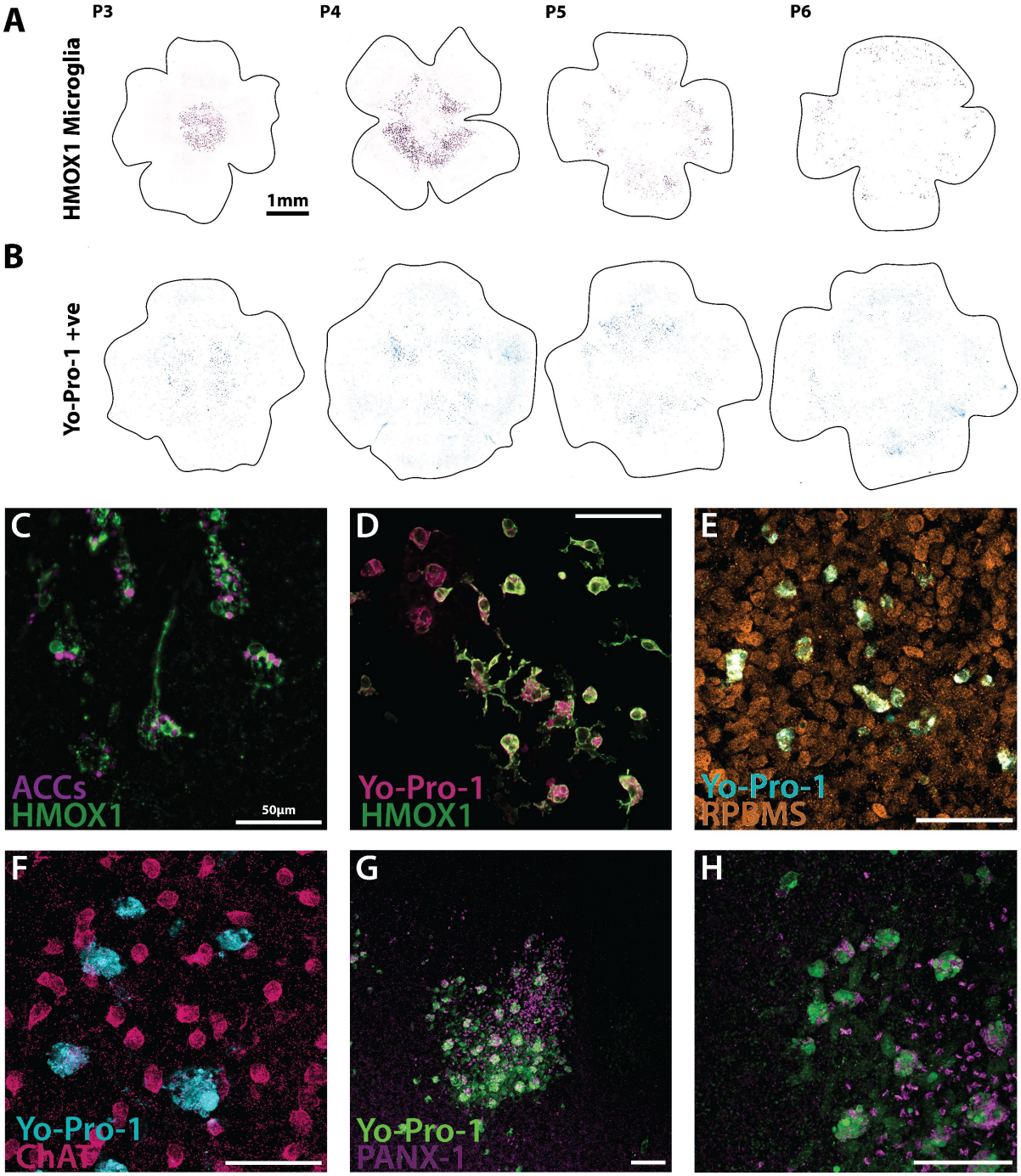


*Figure 4: ACCs are composed of dying RGCs engulfed by Hmox1 expressing microglia* **A.** Mouse retinal wholemounts displaying a subtype of microglia labelled by Hmox1 which sit as an annulus astride the ACCs locations and the SVP. **B.** Mouse retinal wholemounts displaying apoptotic cells labelled with YO-PRO-1 in the periphery and overlapping with the microglia annulus. Scale bar 1mm. **C.** Example Hmox-1 positive microglia with ACCs present inside intracellular vacuoles responsible for breaking down and storing apoptotic cells. **D.** Apoptotic cells labelled with YO-PRO-1 are surrounded by Hmox-1 ramified microglia which become activated and engulf dying cells storing them in intracellular vacuoles similar to AAC storage. **E.** Apoptotic cells labelled with YO-PRO-1 show complete overlap with RGC marker RPBMS. **F.** Apoptotic cells labelled with YO-PRO-1 show no colocalisation with SAC marker ChAT. **G.** PANX-1 hemichannels location tightly overlaps with a cluster of YO-PRO-1 positive cells. **H.** Higher magnification inset of E displaying the tight association between YO-PRO-1 positive cells and PANX-1 hemichannels. Scale bar 50µm.

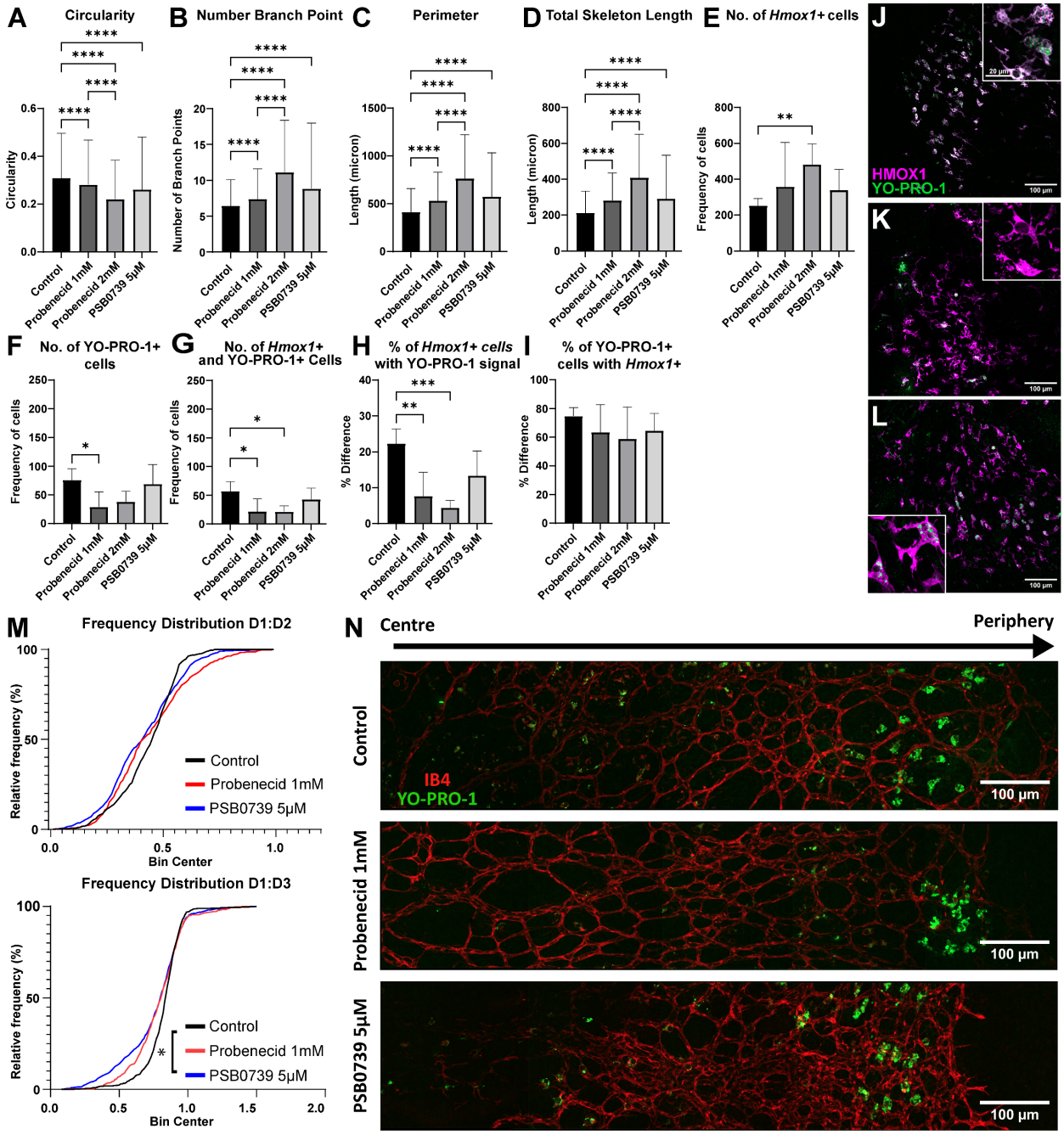


*Figure 5: Purinergic signalling through PANX-1 hemichannels and P2Y12 receptors influences Hmox1 microglia activation at P4.*Quantification of microglial morphology at P4 under control conditions (black bars) and following pharmacological inhibition using Probenecid 1 mM (darkest grey), Probenecid 2mM (medium grey), and PSB0739 5µM (light grey) for 24 hours. Statistical analysis was conducted using one-way ANOVA followed by Tukey's multiple comparisons test. Data are presented as mean ± SEM; *$p < 0.05$, **$p < 0.01$, ***$p < 0.001$, ****$p < 0.0001$. n= 8-10 retinas per group. Cells per group: control= 6829, Probenecid 1mM= 5401, Probenecid 2mM= 4266, and PSB0739 5µM= 3099. **A.** Circularity was significantly reduced in Probenecid 2 mM, and PSB0739 5µM compared to control. **B.** Probenecid and PSB0739 in general significantly increased the number of branch points compared to control. **C.** Cell perimeter was significantly increased by Probenecid 2mM and PSB0739 5µM relative to Control. **D.** Total skeleton length was significantly higher in Probenecid and PSB0739 5µM compared to Control. **E.** Total number of Hmox1 positive cells observed after incubation of probenecid (1mM or 2mM), or PSB0739 5µM for 24 hours prior to fixation and immunolabelling. **F.** Total number of YO-PRO-1 positive cells observed after incubation of probenecid (1mM or 2mM), or PSB0739 5µM for 24 hours prior to fixation and immunolabelling. **G.** Total number of double positive YO-PRO-1 and Hmox1 cells observed

after incubation of probenecid (1mM or 2mM), or PSB0739 5μM for 24 hours prior to fixation and immunolabelling. **H.** Percentage of Hmox1+ cells that co-localise with YO-PRO-1 signal, after incubation of probenecid (1mM or 2mM), or PSB0739 5μM for 24 hours prior to fixation and immunolabelling. **I.** Percentage of YO-PRO-1 positive cells that express Hmox1, representing the proportion of apoptotic cells associated with Hmox1 positive microglia after incubation of probenecid (1mM or 2mM), or PSB0739 5μM for 24 hours prior to fixation and immunolabelling **J.** Micrograph displaying overlap of apoptotic cells labelled with YO-PRO-1 and HMOX-1 positive microglia with higher magnification inset indicated by asterisk. **K.** Micrograph displaying reduced overlap of apoptotic cells labelled with YO-PRO-1 and HMOX-1 positive microglia after 24hr incubation with Probenecid 2mM with higher magnification inset indicated by asterisk. **L.** Micrograph displaying reduced overlap of apoptotic cells labelled with YO-PRO-1 and HMOX-1 positive microglia after 24hr incubation with PSB0739 5μM with higher magnification inset indicated by asterisk. Scale bar = 100μm. Inset scale bar = 20μm **M.** Top- Cumulative frequency distributions of apoptotic cells D1/D2 ratio. N=3344. Bottom- Cumulative frequency distributions of apoptotic cells: D1/D3 ratio Key: Control (black), Probenecid-treated (red), PSB0739-treated (blue). N=3344. **N.** Top- Representative image of P4 mouse retinal whole-mounts showing the SVP (IB4, red) and apoptotic cells (YO-PRO-1, green) across the centre-peripheral axis gradient from left (ONH region) to right (vascular leading edge). Middle- Retina incubated in probenecid for 24hrs (1mM). Bottom- Retina incubated in PSB0739 (5μM) for 24hrs. Scale bars = 100μm.

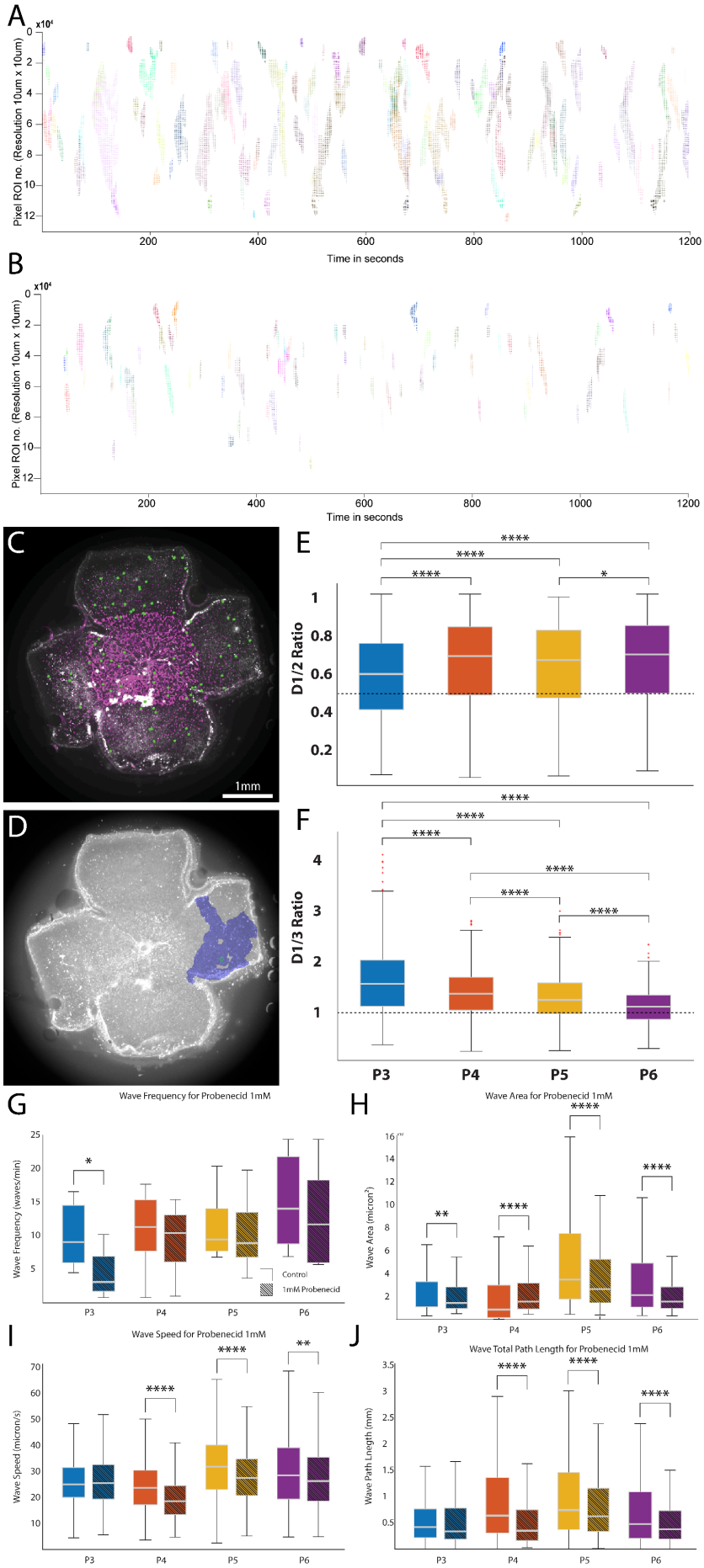
A
B
Pixel ROI no. (Resolution 10um x 10um)
Time in seconds
C
1mm
D
E
D1/2 Ratio
F
D1/3 Ratio
P3
P4
P5
P6
G
Wave Frequency for Probenecid 1mM
Wave Frequency (waves/min)
Control
1mM Probenecid
H
Wave Area for Probenecid 1mM
Wave Area (micron²)
I
Wave Speed for Probenecid 1mM
Wave Speed (micron/s)
J
Wave Total Path Length for Probenecid 1mM
Wave Path Lnegth (mm)

Figure 6: Centrifugal Progression of Retinal Wave Origination is Driven by PANX1-Mediated Purinergic Signalling. **A.** Calcium retinal waves plots of waves in control conditions. Each row represents a pixel ROI (10µm x 10µm) within the calcium imaging recording. Waves are indicated by synchronised activity across channels. The activity is shown against time (in seconds). **B.** Probenecid 1mM profoundly reduces retinal excitability, with significant decrease in wave frequency and number of channels recruited within waves. **C.** Mouse retinal wholemount (P4) displaying superior vascular plexus (SVP) (labelled with isolectin B4 (IB4)) and the origin points of spontaneous retinal waves recorded with calcium imaging (green spots). **D.** Example propagation extent of a retinal wave. **E.** Retinal wave origination becomes increasingly more peripheral (D1/2 > 0.5) over the P3-P6 period. **F.** Retinal waves originate in the non-vascularised more peripheral regions (D1/3 > 1) of the retina regardless of age. **G.** Retinal wave frequency increases from P3-P6 while ATP release blockade with probenecid reduces frequency across the board. **H.** Wave retinal area coverage is reduced significantly by probenecid treatment. **I.** Retinal wave propagation speed is reduced by probenecid treatment in the later stage of first postnatal week. **J.** Retina wave path length increases from P3-5 and is significantly reduced by probenecid treatment. Statistical analysis was conducted using Man-Whitney rank sum test. *p < 0.05, **p < 0.01, ***p < 0.001, ****p < 0.0001.

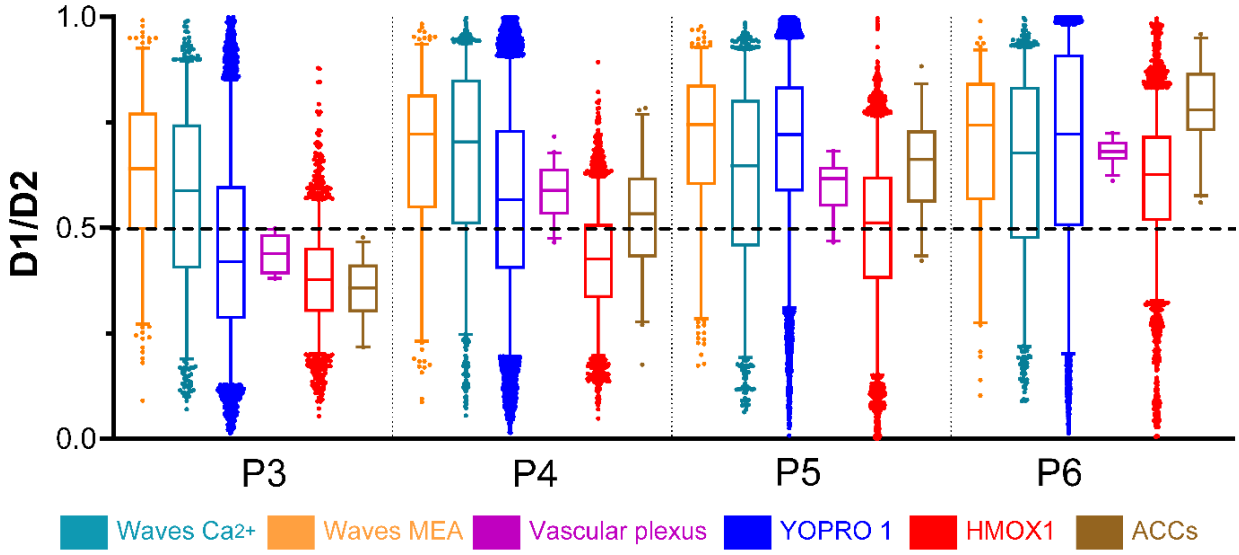


*Figure 7. Relative Peripherality of Multiple Developmental Processes Is Age Invariant.* Box plot showing developmental changes in D1/D2 peripherality ratios for stage II retinal waves recorded by MEA, and calcium imaging, SVP extent, YO-PRO-1 labelling, HMOX-1 microglia locations, and ACCs. Each box illustrates the median (horizontal line) and interquartile range, with minimum and maximum values (whiskers). The distribution of each marker of interest increases in peripherality (D1/2 > 0.5) over the P3-P6 period, see Figure S2.

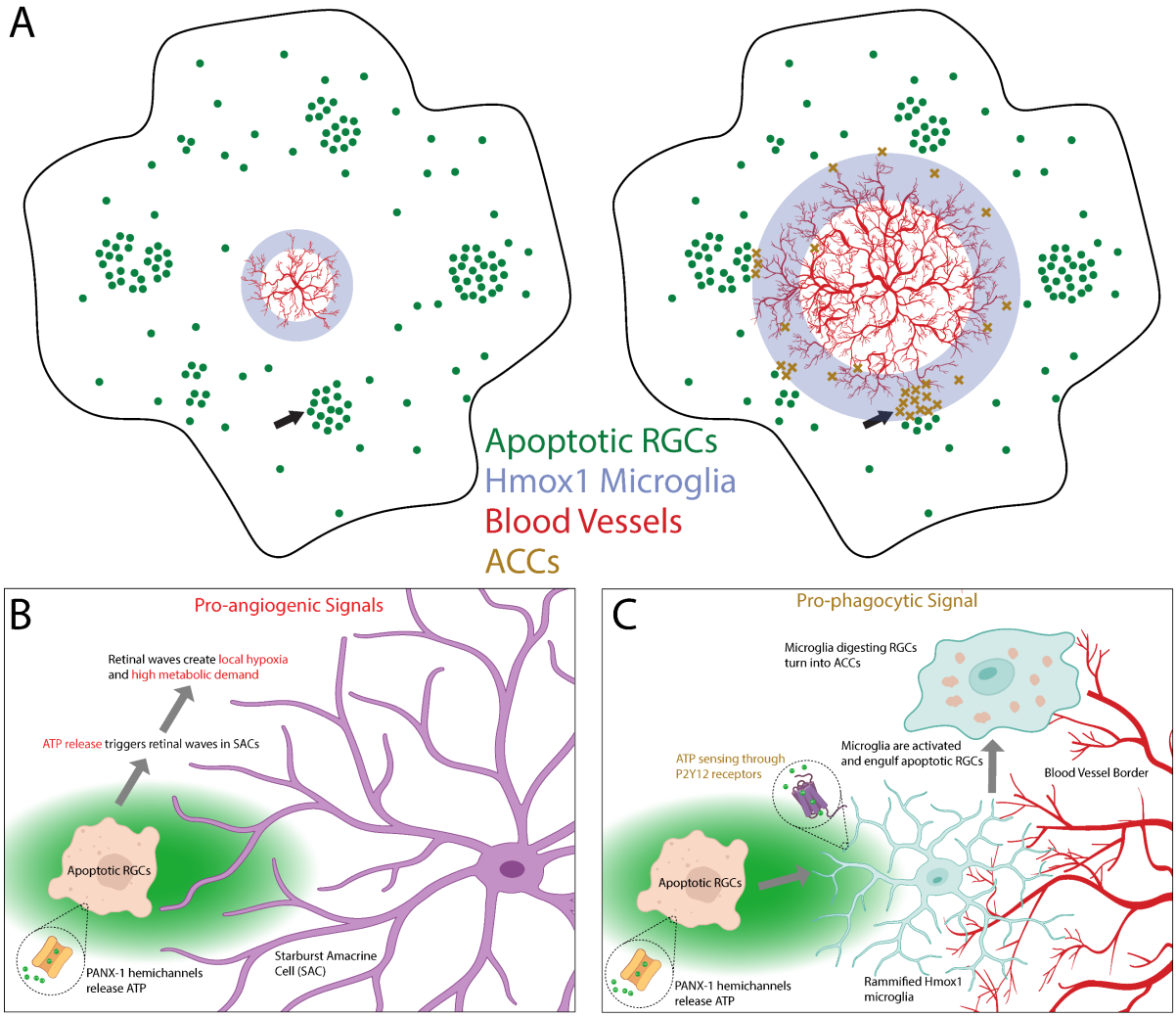


*Figure 8: Overview of Synchronised Development in Retina* **A.** Diagram of a retina at two different timepoints displaying the organisation of apoptotic RGCs, the SVP, the annulus of Hmox1 microglia, and ACCs. Arrows indicate areas explored in higher detail in B,C. **B.** Pro-angiogenic and spontaneous activity phase of the apoptotic RGCs releasing purinergic markers through PANX-1 hemichannels. **C.** Phagocytic phase where Hmox1 microglia sense apoptotic RGCs and engulf them for destruction, creating ACCs.

**Supplementary Info**

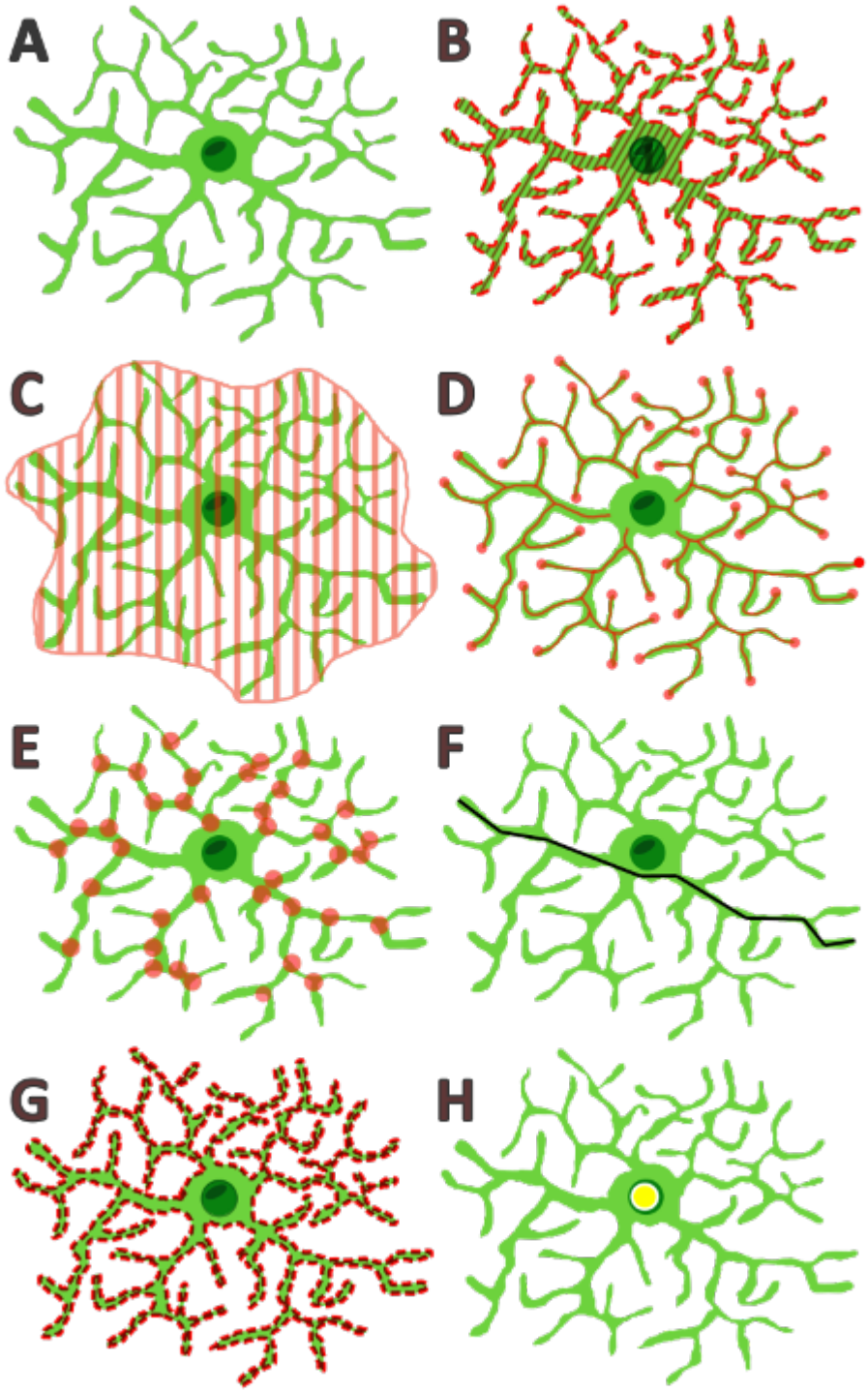


**Figure S1: Microglial Morphometric Parameter Measurements.**

**A.** Microglial cell shape example, **B.** Area of the cell is illustrated by red stripes covering the cell. **C.** Convex Area illustrated by area covered in red stripes, **D.** Length of individual branches- shown by a red line and red dot at the end point of each measurement, **E.** Number of branch points shown by a red dot covering every branch intersection, **F.** Geodesic diameter

highlighted by a black line along the shortest path through the maximum distance of 2 points of the microglia cell, **G.** Perimeter of the cell show by a dashed red line around the cell outline, **H.** The geometric centre of the cell is represented by a yellow circle.

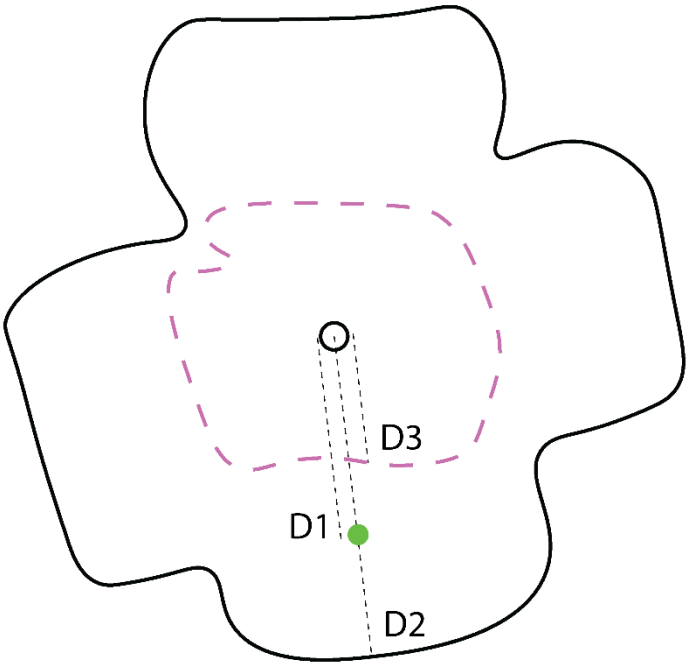


**Figure S2: Peripherality and Vascular Relation Metrics**

Method for calculating the relative position of anatomical markers between the ONH (small black circle in the middle) the periphery, and the vascular plexus. Anatomical markers such as ACCs are represented by a green dot. D1: distance from centre of ONH to the object of interest. D2: distance between the object of interest to periphery. D3: The distance from the ONH through the line of the object of interest to the vascularised border. D1/2 value greater that 0.5 equates to the periphery of the retina. D1/3 value greater than 1 equates to the non-vascularised area of the retina.